Determination of an improved intermolecular global potential energy surface for Ar–H_2O from vibration–rotation–tunneling spectroscopy

R. C. Cohen[a] and R. J. Saykally
Department of Chemistry, University of California, Berkeley, California 94720

(Received 29 September 1992; accepted 29 December 1992)

A new highly accurate and detailed intermolecular potential surface for Ar–H_2O is derived by a direct nonlinear least squares fit to 37 far infrared, infrared, and microwave spectroscopic measurements. The new potential (denoted AW2) gives a much better description of the strong radial dependence of the anisotropic forces and of the binding energy than its predecessor, the AW1 surface [Cohen and Saykally, J. Phys. Chem. **94**, 7991 (1990)]. The global minimum on the AW2 potential (D_e=142.98 cm^{-1}) occurs at the position R=3.636 Å, θ=74.3°, and ϕ=0°. At these coordinates the argon is located in the monomer plane between the perpendicular to the C_2 axis (θ=90°) and the hydrogen bonded geometry (θ=55°). This orientation of the minimum is opposite of that found in recent *ab initio* calculations of Bulski *et al.* [J. Chem. Phys. **94**, 8097 (1991)] and Chalisinski *et al.* [J. Chem. Phys. **94**, 2807 (1991)]. Both sets of authors find a minimum at an antihydrogen bonded geometry corresponding to an orientation Ar–OH (θ=125°).

INTRODUCTION

Anisotropic intermolecular forces govern the behavior of an enormous range of chemical systems. Despite years of study, it is only with the development of methods for directly observing intermolecular vibrations with high precision (i.e., measurement of vibration–rotation–tunneling [VRT] spectra) that significant progress has been made toward quantitative modeling of these forces. Our recent reviews,[1,2] and that of Hutson,[3] provide an overview of state of the art experimental[1] and theoretical[2,3] developments in the study of intermolecular forces. We emphasize the role of far infrared VRT spectroscopy—the most direct probe of the details of intermolecular forces—and new numerical approaches, such as the collocation method, to the study of multidimensional intermolecular dynamics. With the exception of our earlier work describing the intermolecular potential energy surface (IPS) of Ar–H_2O,[4] the most extensive studies of intermolecular forces have been applied to systems with one or two intermolecular degrees of freedom, viz., rare gas (Rg) pairs,[5] Rg–hydrogen,[3,6] and the Rg–hydrogen halide[3,7,8] systems. Extension to higher dimensions requires both a much more extensive data set and very efficient methods for refining a model potential so that it represents all of the available data. In this paper, we describe a new, improved representation of the three-dimensional intermolecular potential energy surface (IPS) for Ar–H_2O denoted AW2. Here and in a forthcoming paper describing the IPS of Ar–NH_3,[9] we continue our effort to combine precise VRT measurements and new efficient computational methodologies for the quantitative determination of intermolecular forces in multidimensional systems.

It should be emphasized for the unfamiliar reader, that the molecular systems listed above represent the only cases for which detailed models of the intermolecular forces have been developed and tested. Extensive measurements of the VRT spectra of more complex (five and six dimensional) systems recently obtained by Elrod *et al.* for Ar_2HCl,[10] by Dore *et al.* for CH_4–H_2O,[11] and by Loeser *et al.* for $(NH_3)_2$,[12] present a challenge requiring still more efficient computational approaches. We hope that the present work provides a basis for this effort. In addition, the IPS of Ar–H_2O is of interest as a model for systems which exhibit hydrophobic interactions,[13,14] and an accurate IPS will also be useful in the development of quantitative models of vibrational and rotational energy transfer, such as those presented by Ree and Shin.[15]

The AW2 IPS (Figs. 1–3) was derived by a direct nonlinear least squares fit to 37 different VRT measurements. This potential represents a substantial improvement over our initial experimental IPS, denoted AW1.[4] While the essential physics of the AW1 potential has proven to be correct, our recently reported measurements[16] unambiguously establish that the coupling between the angular (θ,ϕ) and radial (R) degrees of freedom described by that surface are far too weak. The coordinate system used to describe the complex is an ordinary Jacobi coordinate system (R,θ,ϕ), with its origin at the center of mass of the water monomer. R describes the vector from the center of mass of the water monomer to the argon atom, θ describes the angle of the C_2 axis of the monomer with respect to the R vector with θ=0 along the C_2 axis in the direction of the hydrogen atoms, and ϕ describes the angle of rotation about the C_2 axis from a reference geometry (ϕ=0°) with all four atoms coplanar. Near the minimum on the surface, these new data require even sharper variations in the minimum energy distance (R_m) as a function the relative orientation (θ,ϕ) of the argon and water subunits than were present in the AW1 surface. These results show that approximate analyses based on the assumption that angular–radial coupling in weakly bonded complexes can be neglected must be regarded with suspicion. For instance,

[a]Present address: Department of Chemistry, Harvard University, Cambridge, Massachusetts 02138.

 0021-9606/93/086007-24$06.00

Lascola and Nesbitt,[17] assume that there is no angular–radial coupling in Ar–H_2O and use a purely angular two-dimensional (θ,ϕ) model to argue that the argon has a substantial effect on the water *intra*-molecular bending potential. However, experimental measurements of Ar–H_2O VRT transitions presented by us in Ref. 16 are in sharp disagreement with the predictions based on this model. Specifically, Lascola and Nesbitt predict the VRT state $\Sigma(1_{11})$ will be observed at *lower* energy than its companion $\Pi(1_{11})$. However, we observed $\Sigma(1_{11})$ above $\Pi(1_{11})$, as we predicted using the AW1 IPS. The exact three-dimensional quantum mechanical calculations described below accurately reproduce all of the available VRT data without invoking any coupling to the water bending coordinate. While this is not direct evidence that such coupling is small, it is sufficient to invalidate the notion that coupling to the monomer bend can be inferred from two-dimensional approximations to the intermolecular dynamics. For further emphasis, we note that angular–radial coupling has also been shown to be essential to an accurate description of the dynamics in Ar–NH_3,[9,18] Ar_2–HCl,[10] and Ar–HCN.[19] The Ar–H_2O complex in no way constitutes an exceptional case; rather, coupled multidimensional dynamics are likely to be an intrinsic feature of dynamics in van der Waals complexes.

The AW2 IPS has a global minimum 142.98 cm^{-1} deep at the coordinates $R=3.636$ Å, $\theta=74.3°$, $\phi=0°$. This is a planar geometry with a somewhat nonlinear hydrogen bond (for comparison, the linear hydrogen bonded structure would have $\theta=55°$, $\phi=0°$). Geometries with the argon in the molecular plane ($\phi=0°$) are more favorable than out of plane structures. Barriers to in-plane rotation are 26.29 cm^{-1} at $R=3.702$ Å, $\theta=0°$, $\phi=0°$ [Ar–H_2O] and 17.18 cm^{-1} at $R=3.518$ Å, $\theta=180°$, $\phi=0°$ [Ar–OH_2]. The hydrogen bonded orientation ($\theta\approx55°$) Ar–HOH is 3.4 cm^{-1} less favorable and requires extension of the van der Waals bond length to $R=3.70$ Å. The antihydrogen bonded geometry Ar–OH_2 ($\theta\approx125°$) is 11.1 cm^{-1} above the global minimum at the much shorter bond length of $R=3.460$ Å. These relative energies are probably known to better than ±5 cm^{-1}. The primary limit to their accuracy is the truncation of the series expansion of the IPS. As can be seen in Fig. 1, both the attractive forces and the repulsive forces are maximized along the hydrogen bonded orientation. As a result, the exact position of the potential minimum depends on small variations in the radial dependence and anisotropy of the attractive and repulsive forces. At different orientations the minimum occurs at widely different intermolecular distances. For instance the minimum at $\theta=37.1°$, $\phi=0°$ of -131.17 cm^{-1} occurs at $R=3.723$ Å while a nearly identical minimum energy occurs along the approach at $\theta=128.6°$, $\phi=0°$, but it occurs 0.282 Å closer, at $R=3.441$ Å. Again, strong angular–radial coupling is a dominant feature of the IPS.

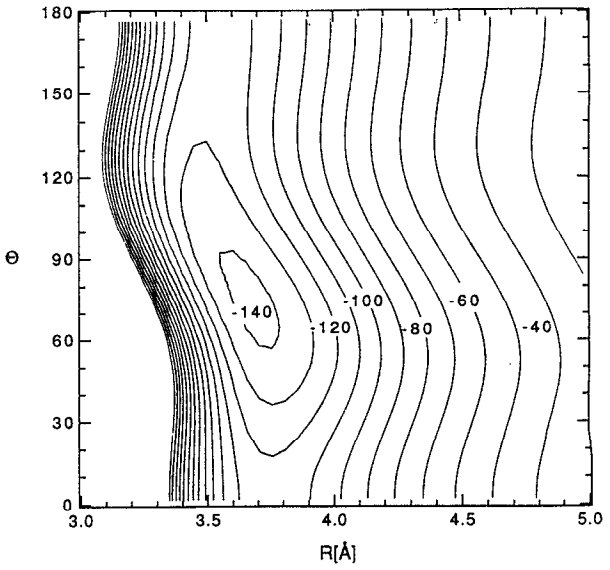

FIG. 1. The AW2 intermolecular potential for Ar–H_2O. R is the vector from the center of mass of the water monomer to the argon and θ is the angle between this vector and the water monomer C_2 axis. For this plot $\phi=0$, constraining the complex to be planar. Contours are drawn at 10 cm^{-1} intervals referenced to a zero of energy at the dissociation energy. Contours above this energy are omitted for clarity.

BACKGROUND

Initial efforts to understand the anisotropic IPS of Ar–H_2O were inspired by our measurements of two internal rotor transitions of the complex.[20] Relying on the assumption of approximate separability of the angular (θ,ϕ) and radial (R) coordinates, Hutson[21] extracted a series of effective two-dimensional angular potential energy surfaces from these measurements. A Coriolis analysis, which we presented in Ref. 13, suggested that the most probable surface was the one with a minimum at the orientation $\theta=90°$, $\phi=0°$, where the water symmetry axis is perpendicular to the van der Waals bond and all four atoms are coplanar. In-plane internal rotation on Hutson's best two-dimensional surface is hindered by barriers of 15 cm^{-1} at both the Ar–H_2O and the Ar–OH_2 C_{2v} configurations, and out-of-plane rotation is hindered by a barrier to internal rotation of 40 cm^{-1} at $\theta=90°$, $\phi=90°$—a geometry with the argon located directly above the plane of the water molecule and along the monomer C_2 axis.

Recently, we developed a new, highly efficient adaptation of the collocation method to obtaining the eigenvalues and eigenvectors of the multidimensional, nonseparable Hamiltonian describing the molecular dynamics of any atom–molecule complex. The computer code for obtaining eigenvalues was then embedded within a nonlinear least squares routine and used to derive a detailed global three-dimensional IPS for Ar–H_2O, (AW1 IPS).[4] This surface, the first accurate and complete treatment of the intermolecular forces in Ar–H_2O, was obtained by a direct fit of a model potential with nine adjustable parameters to the eleven experimental VRT energy differences. Predictions for VRT frequencies made using the AW1 surface have since proven to be quite accurate. The five new VRT bands of Ar–H_2O presented in Ref. 16 were observed at frequencies ranging from 2 to 50 GHz (0.06–1.7 cm^{-1} 0.5%–3%) from the predictions. Lascola and Nesbitt[17] have reported the energy difference between the Σ and $\Pi(1_{01})$ states as

339.763(9) GHz—within 1% (−3.8 GHz) of our predictions. These measurements represent a comprehensive test of the AW1 IPS. The success of these predictions confirms that the essential physics of the weak interaction between argon and water is accurately described by this surface. The AW1 surface has a broad, flat minimum at the planar T-shaped geometry (D_e=174.7 cm^{-1} at R=3.598 Å, θ=85.7°, ϕ=0°), and a barrier at θ=90°, ϕ=90°, which are qualitatively similar to those on Hutson's two-dimensional surface. The barriers to motion of the argon in the plane of the H_2O monomer are 17 cm^{-1} at the Ar–OH_2 (θ=0°, ϕ=0°) geometry and 22 cm^{-1} at the Ar–H_2O geometry (θ=180°, ϕ=0°). The barrier to out-of-plane rotation on the AW1 surface is 47 cm^{-1} (θ=90°, ϕ=90°). On the AW2 surface these barriers are similar but in the opposite sense; it is more difficult (26.3 cm^{-1}) to rotate past the Ar–H_2O configuration than the (17.2 cm^{-1}) Ar–OH_2 configuration.

The full three-dimensional analysis yields insights not available from purely angular potentials. The origin of angular–radial coupling is clearly evident in both the AW1 and AW2 potentials. On the AW1 surface, the long range forces favor the hydrogen bonded geometry and approaches along the C_2 axis. At short range, the repulsive forces on the AW1 surface are weakest at the orientation with argon approaching along the C_2 axis in the plane of the monomer. The barrier to out-of-plane motion arises from the decrease in attractive forces as the argon is rotated out of the plane of the monomer. The repulsive forces favor out-of-plane configurations more than they do in-plane ones. On the AW1 surface, the short range minimum occurs with argon located nearest to the oxygen. Over distances from 3.5–3.8 Å, the optimum orientation shifts from the antihydrogen bonded orientation Ar–OH_2 to the hydrogen bonded one Ar–HOH. This structure in the IPS is the cause of the large angular–radial coupling manifested in the VRT spectra presented in Ref. 16. On the AW2 surface these basic qualitative features persist, although they differ in detail.

There has also been considerable interest in computing the IPS of Ar–H_2O by *ab initio* methods. Chalisinski *et al.*,[22] have computed the interaction energy for Ar–H_2O on a grid of points, using a many-body perturbation theory technique and large basis sets. These authors set a lower limit to the absolute well depth of 108 cm^{-1} and suggest that the true well depth is as much as 25% deeper. This value is considerably smaller than the well depth on the AW1 surface (174.7 cm^{-1}) but is within 10% of the AW2 minimum (143.0 cm^{-1}). Both the attractive and repulsive anisotropies calculated by these authors are dominated by interactions localized near the hydrogen atoms. The authors show that these forces are nearly equal in magnitude and opposite in sign at the potential minimum. The net result obtained by Chalisinski *et al.* is qualitatively similar to that obtained in the two-dimensional analysis of Hutson[21] and to the three-dimensional AW1 IPS. However, the calculations do not appear to be accurate enough to use as a constraint on any aspect of the empirical surface derived below. The minimum on the *ab initio* surface is very

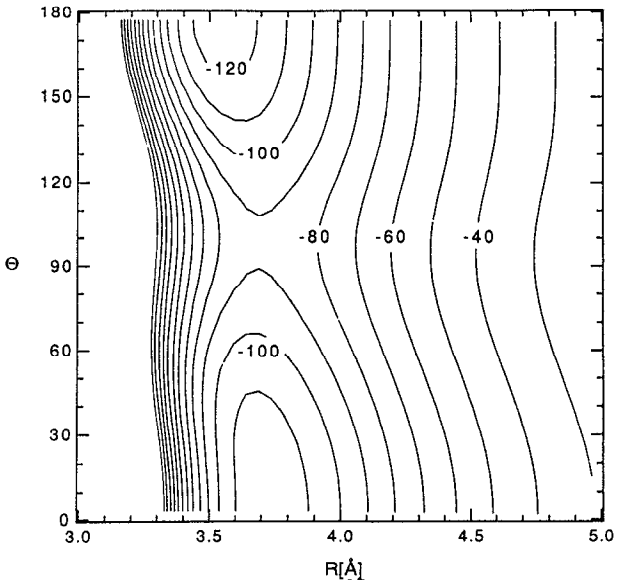

FIG. 2. The AW2 intermolecular potential surface [ϕ=90°].

flat, varying by less than 2 cm^{-1} for geometries with the argon in the plane of the H_2O and oriented in any fashion between the linear hydrogen bonded structure and the T-shaped configuration. There is also a substantial barrier to out-of-plane motion on the *ab initio* potential. As in the AW1 surface, the *ab initio* potential evidences long range attractive forces favoring the linear hydrogen bonded geometry. However, the short range repulsive forces in the *ab initio* calculations are weakest in the threefold hollow formed by the two hypothetical sp^3 hybridized lone pairs and one hydrogen atom of the water molecule. This repulsion is more structured than the parameters of the AW1 IPS permitted, and is consistent with the experimental evidence presented in Ref. 16 for the existence of an angular–radial coupling stronger than that present in the AW1 surface. Another interesting feature of the IPS noted by Chalisinski *et al.* is that no evidence for *localized* sp^3 hybridized lone pairs appear in the *ab initio* calculations. Such structure was not present in the AW1 surface. However, there is some indication of localized lone pairs in the AW2 surface. In Fig. 2, we show a cut through the AW2 IPS in the plane containing the lone pairs. The repulsive wall does extend further from the center of mass at θ=125°—the position of a lone pair orbital—than it does in between the two lone pairs. This is suggestive of the importance of localized lone pairs in the short range region of the IPS. However, as we discuss below, the AW2 potential expansion is not sufficiently well converged to unambiguously confirm or contradict the observation of Chalisinski *et al.*

Bulski *et al.*[23] have performed *ab initio* calculations which independently give the induction,dispersion, and repulsion contributions to the global IPS of Ar–H_2O. This IPS has a global minimum 157 cm^{-1} deep at the antihydrogen bonded geometry R=3.39 Å, θ=129°, ϕ=0°. These authors obtain a binding energy that lies within 15%

of both the AW1 and the AW2 dissociation energies. The position of the minimum is in poor agreement with the AW1 and AW2 potentials. Both of the experimental potentials have minima with hydrogens nearest the argon (θ=75°–85°). Bulski *et al.* obtain a number of other results with important implications for the derivation of an empirical IPS, whether or not their quantitative description of the potential is accurate. First, they find that spherical harmonic ($Y_{\lambda\mu}$) expansions of the anisotropic forces are converging very slowly (terms to at least $\lambda=7$ are required for 0.1% accuracy in the interaction energy) with many small contributions from the different terms, and with no one dominant term in the series. This is in contrast to the *ab initio* results presented by these[24] same authors for Ar–NH_3, which suggest that the anisotropy in the Ar–NH_3 IPS is dominated by large repulsive terms proportional to the Y_{10} and the $[Y_{33}-Y_{3\text{-}3}]$ linear combinations of spherical harmonics. Second, Bulski *et al.* find that most of the anisotropic terms for Ar–H_2O are small near the potential minimum, and that several have a radial dependence such that their sign changes in the vicinity of the potential minimum. Given these facts, it is not surprising that there are substantial disagreements among the IPS of Bulski *et al.*, Chalisinski *et al.*, and the experimental AW2 potential. Accurate *ab initio* description of the shape of the intermolecular potential will require calculation of attractive and repulsive anisotropies to within a few cm^{-1}. On the other hand, the experimental AW2 potential accurately represents the leading terms in a series expansion of these forces near the minimum, where it is most rigorously constrained by the experimental data, but it is increasingly less reliable away from the potential minimum. The AW2 surface also does not represent the effect of high order anisotropies. Such anisotropies could possibly contribute significantly to the appearance of the potential minimum, without having any significant effect on the measured eigenvalues.

THE EXPERIMENTAL DATA SET

The observables which are available as constraints on the shape of the IPS for Ar–H_2O include: vibrational band origins, rotational term values, Coriolis splittings, dipole moments, and the Ar–$H_2{}^{17}O$ nuclear quadrupole hyperfine coupling constants. In all, 12 different VRT levels of the normal isotope,[13,16,17,20,25] and four levels of the d_2-isotope (Ar–D_2O)[26,27] have been measured by a combination of far-infrared, infrared, and microwave spectroscopies. There have also been more limited investigation of other isotopes of this complex,[25,26] but these spectra do not provide enough new information to warrant the additional computational effort required for their inclusion in the fits described below. In the calculations, we include information which is available from $J=0$ and $J=1$ term values, unique information from $J=2$ term values, the energy difference $J=8\ \Sigma(2_{12}) < - J=0\Sigma(1_{01})$, the ground state dipole moment and the nuclear quadrupole hyperfine coupling constants for Ar–$H_2{}^{17}O$ in the ground and the first excited internal rotor state. The experimental data set used in the least squares fits is summarized in Table I. The labels used to identify the VRT states of Ar–H_2O are those used in our previous studies. Eigenstates are labeled by J, the total angular momentum, n, the number of quanta of van der Waals stretch excitation (typically we omit reference to n when $n=0$), Ω, the projection of the total angular momentum on the pseudodiatomic axis of the complex and $j_{k_a k_c}$, a label describing the rotational state of the monomer to which the VRT state correlates in the free rotor limit.

We have observed nine VRT bands of Ar–H_2O using the Berkeley tunable far infrared laser/cw planar jet system.[13,16,20] The infrared combination difference $[\Pi(1_{01})\leftarrow\Sigma(1_{01})]$ reported by Lascola and Nesbitt[17] and the microwave measurements of Fraser *et al.*[25] complete the Ar–H_2O data set. The Ar–H_2O VRT levels sampled include the internal rotor level corresponding to $j=0$, all three asymmetric rotor $j=1$, states and one of the five $j=2$ levels. In the stretching coordinate, $n=0$, 1, and 2 vibrational states have been sampled directly or are strongly coupled to the observed internal rotor transitions. This collection of states samples the full range of the angular degrees of freedom. Only the ground state has an energy which is below the classical barrier to out-of-plane rotation, and all of the states have energies above the barriers to in-plane rotation. Subtraction of the zero point energy localized in the radial coordinate changes these conclusions only slightly. After this correction, the ground state of Ar–H_2O is located at an energy roughly isoenergetic with the top of the two separate barriers to in-plane rotation, and the first excited internal rotor level $\Sigma(1_{01})$ is roughly isoenergetic with the top of the barrier to out-of-plane rotation. All of the other states are still well above the barriers. The measured states also extend over a significant fraction of the radial coordinate. The classically allowed region for the $\Pi(2_{12})$ state ranges from 3.2 to 5.3 Å and the average radial distance in the observed VRT states of Ar–H_2O has been shown[16] to range from 3.66 to 3.89 Å. Some care has been required in interpreting the $J=8\Sigma(2_{12})$ energy, since this state is near-resonant (within 1.5 GHz) with $J=8$ $n=1$, $\Pi(1_{10})$ on the AW2 potential. At higher J, the two states cross and $\Sigma(2_{12})$ becomes lower in energy than $n=1$, $\Pi(1_{10})$. Even when they are this close in energy, these two states are not strongly mixed, as indicated by the wavefunctions obtained on the AW2 IPS. Since $\Sigma(2_{12})$ carries most, if not all, of the oscillator strength for transitions from $\Sigma(1_{01})$ to $J=8$ $n=1$, $\Pi(1_{10})$, and since the observed lines were very strong, we conclude that the assignment we presented for transitions to this state in Ref. 16 is correct.

Ar–D_2O VRT spectra sampling the $j=0$ and all three of the $j=1$ states have been obtained by Suzuki *et al.*,[26] who observed the $\Sigma(1_{11})\leftarrow\Sigma(0_{00})$ and the $\Pi(1_{11})\leftarrow\Sigma(0_{00})$ bands, and by Zwart and Meerts[27] who observed $\Pi(1_{01})\leftarrow\Sigma(1_{01})$ and the $\Pi(1_{10})\leftarrow\Sigma(1_{01})$ bands. Because D_2O has rotational constants which are roughly one half those of H_2O, internal rotation in Ar–D_2O is more strongly hindered by the anisotropic component of IPS. After correction for zero point motion localized in the radial coordinate, the ground state of Ar–D_2O is roughly isoenergetic with the barriers to in-plane internal rotation, as is the ground state of the normal isotope. However, and

TABLE I. Ar–H_2O and Ar–D_2O data included in the least squares fits, residuals computed on the AW2 surface and estimated uncertainties used to weight the data as described in the text.[a]

		Experimental	Residuals	unc.
Ar–H_2O Rotational term values (MHz)				
$J=1\leftarrow 0$				
$\Sigma(0_{00})$	$A_2\leftarrow A_1$	5 975.8[b]	−2.0	5.0
$n=1,\Sigma(0_{00})$	$A_2\leftarrow A_1$	5 676.5[b]	0.8	5.0
$\Sigma(1_{11})$	$A_2\leftarrow A_1$	5 971.1	−3.0	5.0
$\Sigma(1_{01})$	$B_1\leftarrow B_2$	5 824.2[b]	−3.7	5.0
$n=1,\Sigma(1_{01})$	$B_1\leftarrow B_2$	5 461.6[b]	13.8	5.0
$\Sigma(1_{10})$	$B_2\leftarrow B_1$	6 052.8[b]	7.2	5.0
$J=2\leftarrow 1$				
$\Pi(1_{11})$	$A_1\leftarrow A_2$	11 467.8	−4.0	10.0
$\Pi(1_{01})$	$B_1\leftarrow B_2$	11 804.8	1.4	10.0
$n=1,\Pi(1_{01})$	$B_1\leftarrow B_2$	10 772.3	−7.6	10.0
$\Pi(1_{10})$	$B_1\leftarrow B_2$	11 855.4	−11.5	10.0
$\Pi(2_{12})$	$B_1\leftarrow B_2$	11 309.8	41.2	60.0
$J=1\leftarrow 1$				
$\Pi(1_{01})$	$B_1\leftarrow B_2$	205.0[b]	0.5	1.0
$n=1,\Pi(1_{01})$	$B_1\leftarrow B_2$	181.0	0.0	1.0
$\Pi(1_{10})$	$B_1\leftarrow B_2$	146.8[b]	−0.5	1.0
$\Pi(2_{12})$	$B_1\leftarrow B_2$	672.3	26.0	20.0
Ar–D_2O) Rotational term values (MHz)				
$J=1\leftarrow 0$				
$\Sigma(0_{00})$	$A_2\leftarrow A_1$	5 591.3[c]	1.2	5.0
$\Sigma(1_{11})$	$A_2\leftarrow A_1$	6 817.3[d]	50.3	50.0
$\Sigma(1_{01})$	$B_1\leftarrow B_2$	5 458.0[c]	3.6	5.0
$J=2\leftarrow 1$				
$\Pi(1_{01})$	$B_2\leftarrow B_1$	11 257.3[e]	1.7	10.0
$\Pi(1_{10})$	$B_2\leftarrow B_1$	11 464.3[e]	−15.7	10.0
Ar–H_2O Vibrational transitions (GHz)				
$n=1,\ \Sigma(0_{00})\leftarrow\Sigma(0_{00})$	$A_2\leftarrow A_1\ J=1\leftarrow 0$	913.00[b]	0.54	0.75
$\Pi(1_{11})\leftarrow\Sigma(0_{00})$	$A_2\leftarrow A_1\ J=1\leftarrow 0$	1110.82	0.49	0.75
$\Sigma(1_{11})\leftarrow\Sigma(0_{00})$	$A_2\leftarrow A_1\ J=1\leftarrow 0$	1225.84	0.33	0.75
$\Pi(1_{01})\leftarrow\Sigma(1_{01})$	$B_1\leftarrow B_2\ J=1\leftarrow 1$	339.76[f]	−0.51	0.75
$\Pi(1_{10})\leftarrow\Sigma(1_{01})$	$B_1\leftarrow B_2\ J=1\leftarrow 0$	637.47[b]	−0.37	0.75
$\Sigma(1_{10})\leftarrow\Pi(1_{01})$	$B_1\leftarrow B_2\ J=0\leftarrow 1$	738.05[b]	0.15	0.75
$n=1,\ \Sigma(1_{01})\leftarrow\Sigma(1_{01})$	$B_1\leftarrow B_2\ J=1\leftarrow 0$	1024.70[b]	0.73	0.75
$n=1,\ \Pi(1_{10})\leftarrow\Sigma(1_{01})$	$B_1\leftarrow B_2\ J=1\leftarrow 0$	1343.79	−1.60	0.75
$\Sigma(2_{12})\leftarrow\Sigma(1_{01})$	$B_1\leftarrow B_2\ J=8\leftarrow 0$	1866.56	−1.27	1.50
$\Pi(2_{12})\leftarrow\Sigma(1_{01})$	$B_1\leftarrow B_2\ J=1\leftarrow 0$	1840.75	0.55	0.75
Ar–D_2O Vibrational transitions (GHz)				
$\Pi(1_{11})\leftarrow\Sigma(0_{00})$	$A_2\leftarrow A_1 J=1\leftarrow 0$	581.24[d]	0.68	0.75
$\Sigma(1_{11})\leftarrow\Sigma(0_{00})$	$A_2\leftarrow A_1\ J=1\leftarrow 0$	626.46[d]	−0.52	0.75
$\Pi(1_{01})\leftarrow\Sigma(1_{01})$	$B_1\leftarrow B_2\ J=1\leftarrow 0$	334.83[e]	2.28	0.75
$\Pi(1_{10})\leftarrow\Sigma(1_{01})$	$B_1\leftarrow B_2\ J=1\leftarrow 0$	425.28[e]	1.70	0.75
Dipole moment and quadrupole coupling constants				
Ar–H_2O				
$\lvert\mu_a\rvert\Sigma(0_{00})$ (Debye)		0.1099[c]	0.016	0.010
Ar–$H_2{}^{17}O$				
$eQq_{aa}\Sigma(0_{00})$ (MHz)		−1.251[c]	−0.023	0.020
$eQq_{aa}\Sigma(1_{01})$ (MHz)		−4.222[c]	−0.188	0.080

[a]Experimental data from Refs. 13, 16, and 20 except where noted.
[b]Included in the fit to derive the AW1 surface.
[c]Reference 25.
[d]Reference 26.
[e]Reference 27.
[f]Reference 17.

in contrast to the results obtained for the normal isotope, the first few excited internal rotor states in Ar–D_2O lie below the classical barrier to out-of-plane internal rotation. Ar–D_2O VRT spectra thus provide a more sensitive probe of the shape of the potential near the minimum than do the corresponding Ar–H_2O spectra. In combination with the extensive Ar–H_2O data set, the Ar–D_2O VRT spectra allow the determination of higher order anisotropies in the IPS since the indirect effects of these terms is larger in the deuterated complex. In contrast, the Ar–H_2O spectra sample to much higher energy, viz., more than two thirds of the energy necessary to dissociate the complex. The excited states of Ar–H_2O are thus a more sensitive probe of the dissociation energy, and of the slope of the repulsive wall, than are low-lying Ar–D_2O states identified by the same labels.

PARAMETERIZATION OF THE IPS

The intermolecular potential for Ar–H_2O is presumed to be adiabatically separable from the high frequency intramolecular vibrational motion of the monomer. Within this approximation, a different global IPS obtains for each monomer vibrational state (and for each isotope). This approximation is expected to be sufficiently accurate to describe the intermolecular forces in Ar–H_2O to about 1 part in 1000. This crude estimate is based on the ratio of the shift in the high frequency monomer band origins in similar complexes (a few cm^{-1}) to the spacing between the $v=0$ and $v=1$ monomer vibrational levels (1800–3000 cm^{-1}). In the future, if we are able to obtain a potential function which is more accurate than 0.1%, it must be considered to be an effective surface, which includes coupling to high frequency monomer vibrations. As in our previous work,[4] we express the IPS of Ar–H_2O as a sum of contributions from the three forces which are known to contribute to the binding of atom–molcule complexes, viz., repulsion, electrostatic induction, and dispersion

$$V(R,\theta,\phi)=V_{\text{repulsion}}(R,\theta,\phi)+V_{\text{induction}}(R,\theta,\phi)+V_{\text{dispersion}}(R,\theta,\phi). \quad (1)$$

For the sake of clarity and formal adherence to the expected theoretical behavior of the long range forces, we have rearranged some of the expressions for the three components of the IPS, but the expressions are essentially mathematically equivalent to those employed in Ref. 4

$$V_{\text{repulsion}}(R,\theta,\phi)=A(\theta,\phi)e^{-\beta(\theta,\phi)[R-R_{\text{ref}}(\theta,\phi)]}, \quad (2)$$

$$V_{\text{induction}}(R,\theta,\phi)=-\sum_{n=6}^{\infty} C_n^{\text{ind}}(\theta,\phi)R^{-n}, \quad (3)$$

$$V_{\text{dispersion}}(R,\theta,\phi)=-\sum_{n=6}^{\infty} C_n^{\text{disp}}(\theta,\phi)D_n(R)R^{-n}. \quad (4)$$

Here $D_n(R)$ is a damping function of the form proposed by Tang and Toennies,[28] and following Hutson,[29] we damp only the dispersion forces. All of the terms in the model IPS which are a function of the angles (A,β,R_{ref}, $C_n^{\text{ind}},C_n^{\text{disp}}$) are expanded in a series of symmetry adapted renormalized spherical harmonics $T_{\lambda\mu}(\theta,\phi)$

$$f(\theta,\phi)=\sum_{\lambda\mu} f_{\lambda\mu}T_{\lambda\mu}(\theta,\phi), \quad (5)$$

where

$$T_{\lambda\mu}(\theta,\phi)=\left(\frac{4\Pi}{2\lambda+1}\right)^{1/2}[Y_{\lambda\mu}(\theta,\phi)+(-1)^{\mu}Y_{\lambda-\mu}(\theta,\phi)].$$

The coefficients $C_{n\lambda\mu}^{\text{disp}}$ and $C_{n\lambda\mu}^{\text{ind}}$ in the series expansions correspond directly (to within a normalization constant) to the coefficients derived in a spherical tensor representation of the intermolecular forces such as those described by Gray and Gubbins[30] and by van der Avoird *et al.*[31] Symmetry constraints on the multipole expansion of the induction and dispersion interactions for any atom–molecule complex allow nonzero coefficients $C_{n\lambda\mu}$ only when both λ and n are even or when both are odd. For the specific case of Ar–H_2O, symmetry also constrains μ to be even.

The IPS defined in Eqs. (1)–(5) is a flexible function constrained to reproduce the known form of intermolecular forces at both long and short range. The unknowns in this function to be determined by fit to the VRT spectra are the coefficients in the series expansions of $A(\theta,\phi)$, $\beta(\theta,\phi)$, $R_{\text{ref}}(\theta,\phi)$, $C_n^{\text{ind}}(\theta,\phi)$, and $C_n^{\text{disp}}(\theta,\phi)$. However, this involves far too many unknowns to vary in a least squares fit, and many of them are not independently determinable. Accordingly, we place several constraints on the empirical surface to obtain a form with a reasonable number of independent unknowns. First, the IPS is constrained to have the proper quantitative behavior at long range by fixing the values for the $C_{6\lambda\mu}$ and $C_{7\lambda\mu}$ induction and dispersion coefficients, using experimental and *ab initio* values for these properties. Expressions for these terms are summarized in Table II. The necessary molecular constants used to evaluate these expressions and for the other calculations described in this paper are collected in Table III. As before, the induction energy is completely fixed using the experimentally determined multipole moments for water (μ,Θ) and the experimental dipole polarizability of argon, (α_{Ar}). The dispersion energy formally depends on the frequency dependent polarizabilities of both partners in a dimeric complex.[31,41] The expressions for the low order dispersion interactions given in Table II are approximations to the exact expressions which instead employ the static polarizabilities of H_2O and the isotropic C_6 coefficient. The C_6 coefficient incorporates some of the effects of the differences between the frequency dependent polarizabilities and the static polarizabilities. We employ an improved estimate of the isotropic C_6 coefficient for the complex, $C_6=53.91$ hartree $(a_0)^6$, compared to the previous value of 55.7 hartree $(a_0)^6$, using the formula given by Buckingham, Fowler, and Hutson[36]

$$C_6^{ab}=\frac{2C_6^{aa}\bar{\alpha}^a C_6^{bb}\bar{\alpha}^b}{C_6^{aa}[\bar{\alpha}^b]^2+C_6^{bb}[\bar{\alpha}^a]^2}, \quad (6)$$

TABLE II. Coefficients of the multipole expansion of the induction and dispersion forces.

Induction

	C_{00}^{ind}	C_{10}^{ind}	C_{20}^{ind}	C_{22}^{ind}	C_{30}^{ind}	C_{32}^{ind}
R^{-6}	$\alpha_{Ar}\mu^2$		$\alpha_{Ar}\mu^2$			
R^{-7}		$\frac{12}{5}\alpha_{Ar}\mu\Theta_{20}$		$\frac{8}{5}\alpha_{Ar}\mu\Theta_{20}\sqrt{\frac{18}{5}}\alpha_{Ar}\mu\Theta_{22}$		

Dispersion

	C_{00}^{disp}	C_{10}^{disp}	C_{20}^{disp}	C_{22}^{disp}	C_{30}^{disp}	C_{32}^{disp}
R^{-6}	C_6		$C_6\frac{\alpha_{20}^{H_2O}}{3\alpha_{00}^{H_2O}}$	$\sqrt{\frac{3}{8}}C_6\frac{\alpha_{22}^{H_2O}}{3\alpha_{00}^{H_2O}}$		

$$\Theta_{20}=\left[\Theta_{zz}-\frac{1}{2}(\Theta_{xx}+\Theta_{yy})\right],\quad \Theta_{22}=(\Theta_{xx}-\Theta_{yy}),$$

$$\alpha_{20}^{H_2O}=\alpha_{zz}-\frac{1}{2}(\alpha_{xx}+\alpha_{yy}),$$

$$\alpha_{22}^{H_2O}=(\alpha_{xx}-\alpha_{yy}),\quad \alpha_{00}^{H_2O}=\frac{1}{3}(\alpha_{xx}+\alpha_{yy}+\alpha_{zz})$$

Here $\bar{\alpha}^a$ is the isotropic polarizability of molecule a and C_6^{aa} is the isotropic dispersion coefficient for the homodimer. The C_6 coefficients used in this work are estimates obtained from measurements of dipole oscillator strength distributions. The C_7 coefficients are taken from the calculations of Bulski *et al.*,[23] which we presume to be more accurate than our previous estimate. Second, we reduce the number of unknowns further by truncating the series expansion of induction forces and dispersion forces at C_9. Truncating the attractive forces places limits on the number of terms which can be included in the spherical harmonic expansion, since the multipole expansion of the induction and dispersion forces obey the constraint $\lambda \leqslant (n-4)$.[30] In any case, the available experimental data do not demand these higher order anisotropies. One strategy for bootstrapping up to higher order dispersion terms has been employed by Hutson in recent studies of Rg–HX potentials.[7,8] By fixing the ratio C_8/C_{10} at a value obtained from *ab initio* calculations, some of the effects of higher order terms may be more accurately accounted for (if the *ab initio* ratio is correct). We have not employed this method here and do not expect that our results would have differed significantly if we had. Third, we subsume the induction forces which are not fixed into the dispersion contribution proportional to the same power of R. The induction and dispersion coefficients which vary as the same power of R are not separately determinable, since they differ in form only by the presence of the damping function (which is a weak function of R in the region sampled by the experimental data) in the dispersion energy. The second and third approximations require that the C_8 and C_9 "dispersion" coefficients be interpreted with some care; again, they reflect the sum of both dispersion and induction forces. More importantly, the values of the C_8 and C_9 coefficients determined in the fits will accurately represent the long range C_8

TABLE III. Physical constants for argon, H_2O, and Ar–H_2O.

$\mu=0.7298\ ea_0$	Reference 32	$\theta_{xx}=1.96\ ea_0^2$ $\theta_{yy}=-1.86\ ea_0^2$ $\theta_{zz}=-0.097\ ea_0^2$	Reference 33
$\alpha_{xx}=10.311\ a_0^3$ $\alpha_{yy}=9.549\ a_0^3$ $\alpha_{zz}=9.907\ a_0^3$	Reference 34	$\alpha_{argon}=11.096\ a_0^3$	Reference 35
$C_6^{argon\text{-}argon}=64.3$ hartree a_0^6	Reference 36	$C_7^{10}=73.4$ hartree a_0^7	Reference 23
$C_6^{H_2O\text{-}H_2O}=45.37$ hartree a_0^6	Reference 36	$C_7^{30}=-13.6$ hartree a_0^7	Reference 23
$C_6^{Ar\text{-}H_2O}=53.91$ hartree a_0^6	See the text	$C_7^{32}=12.3$ hartree a_0^7	Reference 23
Atomic masses (g/mol)	Reference 37		
H=1.007 825	D=2.014 102		
^{16}O=15.994 915	^{17}O=16.999 131	^{40}Ar=39.962 384	
Reduced mass			
Ar–$H_2{}^{16}O$=12.415 189	Ar–$H_2{}^{17}O$=12.884 241	Ar–$D_2{}^{16}O$=13.339 416	
Center of mass coordinates (x,y,z) Å origin at the oxygen atom			
$H_2{}^{16}O$ (0, 0, 0.067)	$H_2{}^{17}O$ (0, 0, 0.063)	D_2O (0, 0, 0.120)	
Watson A-reduced rotational constants (cm^{-1})[a]			
$H_2{}^{16}O$ A=27.880 6	C=9.277 8	B=14.521 6	Reference 38
Δ_j=0.013 846	Δ_{jk}=−0.043 590	Δ_k=0.032 094	
δ_j=0.003 408	δ_k=−0.005 562		
D_2O A=15.420 0	C=4.845 3	B=7.272 9	Reference 38
Δ_j=0.004 001	Δ_{jk}=−0.012 56	Δ_k=0.009 10	
δ_j=0.000 988	δ_k=−0.001 737		
$H_2{}^{17}O$ A=27.6953	C=9.256 8	B=14.521 4	Reference 39

Quadrupole hyperfine coupling constants (MHz)

	$H_2{}^{17}O$ Reference 39	D_2O Reference 40
eQq_{aa}=	−8.891	0.153 9
eQq_{bb}=	−1.224	0.022 1
eQq_{cc}=	10.115	−0.175 04

[a]The rotation and distortion constants for $H_2{}^{16}O$ and D_2O are obtained from a fit to the low j (j=0–4) rotational lines reported in Ref. 38 using the II^r coordinate system ($a\rightarrow x$, $b\rightarrow z$, and $c\rightarrow y$) used in calculations throughout this work.

and C_9 coefficients of the "true" untruncated representation only if the multipole expansion is rapidly converging in the region sampled by the data. Otherwise these constants should not be interpreted physically, since they will reflect contributions from C_{10}, C_{11},$\cdots$ terms in a nonconverging series. If this is the case, they should be viewed simply as parameters of a flexible functional form for the IPS.

These first three constraints still leave too many parameters [36 if all terms through $T_{44}(\theta,\phi)$ are included] to be independently determined from the VRT data. Since the VRT data sample the region of the potential near the minimum, it is useful to express the potential as a series expansion in the angular coordinates about the position of the radial minimum. Building on the treatment of the IPS of Rg–H_2 systems developed by LeRoy and Hutson,[42] and used by Hutson[28] in the development of Rg–HX (X=F, Cl, Br) IPS,[3,7,8,29] we constrain $R_{\rm ref}(\theta,\phi)$ (the reference distance in the exponential repulsion) to be the position of the radial minimum $[R_m(\theta,\phi)]$ along the orientation (θ,ϕ). We constrain the one-dimensional radial cut along the orientation (θ,ϕ), to have a well depth of $-\epsilon(\theta,\phi)$, located at $R_m(\theta,\phi)$,

$$V(R_m,\theta,\phi)=-\epsilon(\theta,\phi), \tag{7}$$

and require the first derivative of the IPS with respect to R to be zero at the minimum,

$$V'(R_m,\theta,\phi)=0. \tag{8}$$

The well depth at the position of the radial minimum $\epsilon(\theta,\phi)$ is then expanded in symmetry adapted renormalized spherical harmonics, as in Eq. (5). In the fits we vary the coefficients of this expansion $(\epsilon_{\lambda\mu})$, rather than the values of $A_{\lambda\mu}$ and the coefficients of the dispersion $C_{8\lambda\mu}$ and $C_{9\lambda\mu}$. This procedure has been shown[42] (and our own tests confirm) to produce a set of potential parameters which are more precisely determined and are less correlated than does a direct fit to the parameters $R_{\rm ref}^{\lambda\mu}$, $A_{\lambda\mu}$, and $C_{n\lambda\mu}$. In all systems (Rg–H_2,[42] Rg–HX,[3,7,8] Ar–NH_3,[9] and in this work) for which the constraint $R_{\rm ref}=R_m$ has been employed and for which $A_{\lambda\mu}$ and $C_{n\lambda\mu}$ have been related to each other through $\epsilon_{\lambda\mu}$, the model potential has retained sufficient flexibility to accurately reproduce the experimental data despite the large reduction in the number of free parameters. We also emphasize that because of the relationship imposed by this parameterization between $C_{n\lambda\mu}$ and $\epsilon_{\lambda\mu}$, the shape of the potential minimum is very insensitive to the choice of values for the C_6 and C_7 coefficients. Changes in these coefficients are easily compensated for by corresponding changes in C_8 and C_9 with virtually no effect on the potential in the region most extensively sampled by the VRT data.

Rearranging Eqs. (7) and (8), defines a nonlinear transformation between the primitive potential parameters $C_8(\theta,\phi)$, $C_9(\theta,\phi)$, $A(\theta,\phi)$and the quantities actually determined in the fit, $\beta(\theta,\phi)$, $\epsilon(\theta,\phi)$, and $R_m(\theta,\phi)$:

$$C_8(\theta,\phi)=\frac{\{\beta(\theta,\phi)[\epsilon_{\rm even}(\theta,\phi)+V_{\rm FIX}^{\rm even}(R_m(\theta,\phi),\theta,\phi)]+V_{\rm FIX}'^{\rm even}(R_m(\theta,\phi),\theta,\phi)\}R_m^8(\theta,\phi)}{[D_8'(R_m(\theta,\phi))-D_8(R_m(\theta,\phi))\{8/R_m(\theta,\phi)-\beta(\theta,\phi)\}]}, \tag{9}$$

$$C_9(\theta,\phi)=\frac{\{\beta(\theta,\phi)[\epsilon_{\rm odd}(\theta,\phi)+V_{\rm FIX}^{\rm odd}(R_m(\theta,\phi),\theta,\phi)]+V_{\rm FIX}'^{\rm odd}(R_m(\theta,\phi),\theta,\phi)\}R_m^9(\theta,\phi)}{[D_9'(R_m(\theta,\phi))-D_9(R_m(\theta,\phi))\{9/R_m(\theta,\phi)-\beta(\theta,\phi)\}]}, \tag{10}$$

$$A(\theta,\phi)=C_8(\theta,\phi)D_8(R_m(\theta,\phi))R_m^{-8}(\theta,\phi)+C_9(\theta,\phi)D_9(R_m(\theta,\phi))R_m^{-9}(\theta,\phi)-V_{\rm FIX}^{\rm odd}[R_m(\theta,\phi),\theta,\phi]$$
$$-V_{\rm FIX}^{\rm even}[R_m(\theta,\phi),\theta,\phi]-\epsilon(\theta,\phi), \tag{11}$$

where

$$V_{\rm FIX}^{\rm even}[R_m(\theta,\phi),\theta,\phi]$$
$$=-C_6^{\rm ind}(\theta,\phi)R^{-6}-C_6^{\rm disp}(\theta,\phi)D_6[R_m(\theta,\phi)]R^{-6},$$

$$V_{\rm FIX}^{\rm odd}[R_m(\theta,\phi),\theta,\phi]=-C_7^{\rm ind}(\theta,\phi)R^{-7}$$
$$-C_7^{\rm disp}(\theta,\phi)D_7[R_m(\theta,\phi)]R^{-7}.$$

In Eqs. (9)–(11), $\epsilon_{\rm even}(\theta,\phi)$ and $\epsilon_{\rm odd}(\theta,\phi)$ refer to sums over only the even or odd λ contributions to $\epsilon(\theta,\phi)$. Expressions for the derivatives of the damping functions are given in Ref. 29. In deriving Eqs. (9) and (10), we have applied the additional constraint that C_8 be proportional to both $\epsilon_{\rm even}$ and $V_{\rm FIX}^{\rm even}$, and that C_9 be proportional to $\epsilon_{\rm odd}$ and $V_{\rm VIX}^{\rm odd}$. This ensures that these two terms vary approximately as λ=even and λ=odd spherical harmonics, respectively. Using Eqs. (9) and (10), it can be shown that if $\beta(\theta,\phi)$ and $R_m(\theta,\phi)$ were isotropic, the relationship would be exact. The accuracy of the approximation depends in detail on the size and shape of the anisotropy in these two terms. For the case of the AW2 IPS this approximation is good to better than 5%. It should be noted that this is a limit only to our ability to physically interpret the C_8 and C_9 values derived from the AW2 parameters. The actual energies defined by the AW2 IPS may be more accurate than this.

The mathematical representation described above for the IPS has a number of differences from the form used to develop the AW1 surface. These differences are primarily aesthetic and the quantitative differences between the two forms are small. The new formulations more closely adhere

to established theoretical treatments of intermolecular forces,[30,31] and have been arranged as much as possible as expansions in renormalized spherical harmonics to facilitate a clearer discussion of the contribution of the different attractive and repulsive terms in the IPS and, specifically, of their relationship to the coefficients $\epsilon_{\lambda\mu}$.

SENSITIVITY ANALYSIS

At this point we are left with a model IPS with the parameters, $\epsilon_{\lambda\mu}$, $R_m^{\lambda\mu}$, and $\beta_{\lambda\mu}$ defined in Eqs. (9)–(11), to be determined through least squares analysis. Before describing the procedure we have employed to develop the full three-dimensional IPS from the experimental data, it is useful to make a qualitative assessment of which terms are determinable from the VRT data set. The existing data consist of VRT energy differences, rotational term values, *l*-type splittings, and expectation values associated with the dipole moment and quadrupole hyperfine structure of the complex. The relationship of these data to the potential parameters described above can be characterized by using formulas derived within the reversed adiabatic approximation for the effect of the radially averaged anisotropies on the internal rotor basis states. As Hutson[21] has shown, the energies of the first four ortho levels in symmetric Ar–H_2O isotopes are given approximately by

$$
\begin{aligned}
E[\Sigma(1_{01})] &= E_{1_{01}} - \epsilon_{00} + \tfrac{1}{5}\epsilon_{20} - \frac{\sqrt{6}}{5}\epsilon_{22}, \\
E[\Pi(1_{01})] &= E_{1_{01}} - \epsilon_{00} - \frac{1}{10}\epsilon_{20} + \frac{\sqrt{6}}{10}\epsilon_{22} \\
&\quad - \frac{1}{4}\frac{(\epsilon_{10})^2}{E[\Pi(1_{10})] - E[\Pi(1_{01})]}, \qquad (12) \\
E[\Pi(1_{10})] &= E_{1_{10}} - \epsilon_{00} - \frac{1}{10}\epsilon_{20} - \frac{\sqrt{6}}{10}\epsilon_{22} \\
&\quad + \frac{1}{4}\frac{(\epsilon_{10})^2}{E[\Pi(1_{10})] - E[\Pi(1_{01})]}, \\
E[\Sigma(1_{10})] &= E_{1_{10}} - \epsilon_{00} + \frac{1}{5}\epsilon_{20} + \frac{\sqrt{6}}{5}\epsilon_{22},
\end{aligned}
$$

where E_{101} and E_{110} refer to the free rotor energies of the unperturbed monomer. These equations neglect the effects of angular–radial coupling, higher order anisotropies (ϵ_{30},ϵ_{32},$\cdots$), and coupling to higher (i.e., with $j \geqslant 2$) internal rotor levels. Within these approximations, the relative energies of these four $j=1$ ortho states determine the coefficients, $|\epsilon_{10}|$, ϵ_{20}, and ϵ_{22} in the potential expansion.

Similar analysis shows that the energies of the Σ and $\Pi(1_{11})$ para states are most sensitive to $|\epsilon_{10}|$, and to ϵ_{20}. The measurement of these transitions provides independent confirmation of the values of the parameters, which are otherwise specified by the ortho $j=1$ levels, and allows the effects of higher order terms to be evaluated. In particular, the Ar–H_2O $\Sigma(1_{11})$ state is strongly affected by angular–radial coupling. Since the well depth parameters are established by the Ar–H_2O ortho levels, the position of the para levels establishes the variation in the position of the radial minimum with orientation (primarily the parameters $R_m^{\lambda\mu}$, but also $\beta_{\lambda\mu}$). The measured Σ and $\Pi(2_{12})$ states provide the data which may allow determination of $|\epsilon_{30}|$ and $|\epsilon_{32}|$, since these terms mix $j=2$ internal rotor states with (among other states) the measured $j=1$ internal rotor levels. Without the $j=2$ internal rotor levels the contribution of the small ($\sim$20 cm^{-1}) $|\epsilon_{30}|$ and $|\epsilon_{32}|$ terms to the $j=1$ internal rotor energies cannot easily be separated in the fits from the effects of lower order anisotropies. The Ar–D_2O $j=1$ internal rotor energies are sensitive (to first order) to the same potential parameters as the Ar–H_2O $j=1$ energies. Differences in the effect of second order contributions and in the zero point motions along the radial coordinate allow higher order terms in the spherical harmonic expansion of the well depth and some of the parameters $R_m^{\lambda\mu}$ and $\beta_{\lambda\mu}$ to be established.

The parameter ϵ_{10} and likewise all other coefficients of λ=odd spherical harmonics enter into the energy expressions as a square (i.e., they do not contribute to any diagonal matrix elements). The signs of these terms in the potential is thus not directly determinable from the position of the VRT band origins. In the final AW2 potential, we include two λ=odd terms, viz., ϵ_{10}, and ϵ_{30}. Four different potentials, corresponding to all possible combinations of the signed values of these parameters might possibly yield equivalent fits to the experimental vibrational eigenvalue differences. The signed value of the dipole moment does place restrictions on the signed values of these terms. Hutson[21] has given a clear exposition of the relationship of the ground state dipole moment to the signed value of ϵ_{10}. The dependence on the signed value of ϵ_{30} can be derived in an analogous fashion. However, only the magnitude of the ground state dipole moment has been measured, not its sign.[25] The ambiguity in the sign of these coefficients is thus not resolved by these measurements either. Despite this problem, knowledge of the absolute magnitude of the dipole moment does constrain the relative signed values of the terms. For instance, since the dipole moment of Ar–H_2O in its ground state is small, a large positive value of ϵ_{10} (which would contribute to a large positive dipole moment) requires that ϵ_{30} have a large negative value to compensate, and produce a small net dipole moment. Hence, the magnitude of the dipole moment does reduce the fourfold indeterminacy—even without knowledge of its sign. Rotational term values, isotope shifts, and nuclear quadrupole hyperfine coupling constants also can be weakly sensitive to the sign of the coefficients of odd spherical harmonics. The nuclear quadrupole coupling constants of Ar–$H_2{}^{17}O$ measured in the microwave experiments of Fraser *et al.*[25] are useful in this respect. These data are mainly sensitive to the values of ϵ_{20} and ϵ_{22}, although they will be weakly sensitive to other potential parameters.

The $n=1 \leftarrow n=0$ stretching frequencies are sensitive to the curvature of the IPS near the minimum. This curvature depends primarily on the parameters describing the isotropic well depth (ϵ_{00}) and the slope of the repulsive wall (β_{00}). Measurement of the fundamental stretching fre-

quency does not allow both of these parameters to be determined independently, even though a correlated combination of the two is very precisely determined. In the absence of a direct measure of the dissociation energy, decoupling these two parameters requires measurement of more than two points on the potential curve. Higher stretching levels, internal rotor levels which are mixed with higher stretching levels, or VRT data for different isotopes can provide the necessary constraints. Alternatively, nonspectroscopic data such as the temperature dependence of pressure second virial coefficients could be used as a constraint. This has proven effective in our recent study of the IPS of $Ar–NH_3$.[9]

The rotational energy level differences provide a measure of the expectation value of $1/R^2$, which in turn is most sensitively dependent on the potential parameters $R_m^{\lambda\mu}$, although they are weakly dependent on the parameters $\beta_{\lambda\mu}$ as well. A single $J=1\leftarrow 0$ rotational term value specifies the isotropic term, and additional ones specify anisotropic contributions to the extent that they cannot be reproduced by the isotropic term. Three anisotropic terms were sufficient to reproduce the experimental data used to derive the AW1 potential. The additional data now available require the inclusion of two more terms. The other VRT data now available are l-type splittings in the Π states which result from Coriolis mixing with Σ internal rotor states. In the absence of angular–radial coupling, l-type splittings provide little information which is not also contained in vibrational band origins and rotational term values. Since l-type splittings are a precise probe of the VRT wave function, the extent that they are not exactly reproduced by the same terms which specify the band origins and rotational term values of the states involved can determine higher order anisotropic terms in the well depth expansion. However, in $Ar–H_2O$ the effects of higher order well depth anisotropies on the l-type splittings are small. The l-type splittings also specify the extent of angular–radial coupling, as we demonstrated in Ref. 16. As do the other data which are sensitive to angular–radial coupling, the Coriolis splittings determine the potential parameters $R_m^{\lambda\mu}$. In the case of $Ar–H_2O$, these Coriolis splittings provide a more precise constraint on the angular–radial coupling in the IPS than do the positions of the VRT states alone. This can be seen in the magnitude of the relative errors of the predicted values for these properties on the AW1 surface. Although the largest error in the predicted position of a VRT band is 3%, errors of more than 50% in the l-type splittings are evidenced.

COMPUTATIONAL METHODS

Accurate calculation of the eigenvalues and eigenvectors corresponding to the multidimensional intermolecular dynamics that occur within van der Waals clusters remains the major impediment to extracting experimental IPS from VRT spectra. Only the close-coupling approach[3,7,8,43] and the collocation method[4] have been embedded in a nonlinear least squares loop for the purpose of directly fitting of VRT data to a model IPS. However, other methods[44–46] might actually be the most efficient for certain problems. Two recently developed methods, the DVR[44,45] and the collocation method[4,47–50] are closely related. Both are members of a class of numerical methods known as mixed basis set/pointwise techniques and have the advantage that no integrals are required for evaluation of matrix elements. The collocation method is perhaps the simpler of the two to implement. In addition to its simplicity, the primary advantage of the collocation method is that it can incorporate nondirect product basis functions. For example, Yang and Peet[50] used a local basis set of distributed Gaussian functions in R and in θ in their computations of the eigenvalue spectrum of $Ar–CO_2$. If a direct product basis set were used, every function in R would be paired with every function in θ. However, by placing functions only at points where the potential energy is below some fixed cutoff value, equivalent convergence can be achieved with a much smaller basis set. Because of the large repulsive anisotropy, points below the cutoff are not distributed spherically about the center of mass of the CO_2 and a nondirect product basis set (viz., every function in the radial coordinate is not paired with every function in the ϕ coordinate) results.

In our own work we have employed another set of nondirect product functions, the Wigner D matrices, $D(\chi,\theta,\phi)$. The spherical harmonics $Y_{\lambda\mu}(\theta,\phi)$ and the Wigner D matrices are natural basis functions for many van der Waals clusters with three or more internal degrees of freedom because of the large amplitude motions that occur in the angular coordinates. In this basis, every function in the azimuthal coordinates (ϕ,χ) is not paired with every function the coordinate θ, in these functions. Specifically, only the functions $Y_{\lambda\mu}(\theta,\phi)$ with $|\mu|$ less than λ exist. A direct product basis would thus require inclusion of such obviously irrelevant functions as $Y_{2,10}$. The advantage of being able to employ such nondirect product basis sets that is inherent to the collocation method allows considerable reduction in the size of the basis set compared to what would be necessary in a DVR calculation. On the other hand, Light and co-workers[44,45] have developed elegant schemes for truncation, diagonalization, and recoupling within the DVR framework that allow solution of large eigenvalue problems by the successive evaluation of small matrices. This is a powerful advantage, one which in some cases may outweigh the penalty of using a larger than optimal basis set. Equivalent techniques have not yet been developed in conjunction with the collocation method. The iterative procedure described by Yang and Peet[50] for use with diagonally dominant matrices is one step in this direction.

The collocation equations

The essential procedures for the calculation of atom–polyatom eigenvalues and eigenvectors through the application of the collocation method were described in Ref. 4. A brief review is presented here along with details of improvements and additions to the methodology developed since our initial extension of the method to three dimensions. These include the use of contracted radial basis functions, an improved algorithm for distributing points in the

angular coordinates, and the use of the eigenvectors to calculate the expectation values of various operators.

The Ar–H_2O complex is embedded in a body-fixed Jacobi coordinate system with the origin at the center of mass of the H_2O and the body-fixed z axis localized along the vector R, which connects the H_2O center of mass to the atom. The angles θ and ϕ are the Euler angles describing the position of the argon with respect to a molecule-fixed Cartesian coordinate system with z' along the C_2 axis and the x' axis in the plane of the monomer. θ describes the angle between the H_2O C_2 axis and the vector R, and ϕ describes internal rotation of the H_2O about its C_2 axis. The reference frame is chosen such that $\phi=0°$ when all four atoms are coplanar and $\theta=0°$ when the argon lies on the C_2 axis closest to the hydrogens. The angles α, β, and γ are the Euler angles used to describe the orientation of the pseudodiatomic frame of the complex (the R vector) with respect to the laboratory frame space-fixed axis system. The Hamiltonian for Ar–H_2O in these coordinates is expressed as

$$H=\frac{\hbar^2\partial^2}{2\mu R^2\,\partial R^2}R+\frac{\hbar^2}{2\mu R^2}(\hat{J}^2+\hat{j}^2-2\hat{j}\cdot\hat{J})+H_{\text{monomer}}+V(R,\theta,\phi), \tag{13}$$

where the H_{monomer} we employ a phenomenological Hamiltonian capable of reproducing the rotational energies ($j=0-2$) of H_2O (or D_2O) in its ground vibrational state to better than 0.003 cm^{-1}. Errors in the calculated monomer energies make a negligible contribution to the total uncertainty in the calculation of energies of the complex. The Hamiltonian employed here is a standard Watson A-reduced Hamiltonian including the effects of the quartic centrifugal distortion operators. Without inclusion of the effects of quartic centrifugal distortion, the rotational energies of the $j=0$–2 levels of water are not reproduced to better than 0.1 cm^{-1}

$$H_{\text{monomer}}=\left(\frac{A+C}{2}\right)\hat{j}^2+\left[B-\left(\frac{A+C}{2}\right)\right]\hat{j}_z^2+\left(\frac{A+C}{4}\right)(\hat{j}_+^2+\hat{j}_-^2)-\Delta_j\hat{j}^4-\Delta_k\hat{j}_z^4-\Delta_{jk}\hat{j}^2\hat{j}_z^2-2\delta_j\hat{j}^2(\hat{j}_+^2+\hat{j}_-^2)-\delta_k[\hat{j}_z^2(\hat{j}_+^2+\hat{j}_-^2)+(\hat{j}_+^2+\hat{j}_-^2)\hat{j}_z^2]. \tag{14}$$

For the calculations described in this work we have chosen the monomer z axis to be the symmetry axis. However, the rotational and distortion constants of Ref. 38 are defined with the monomer a axis as the z axis. In order to make use of the distortion Hamiltonian it was necessary to refit the experimental data for water in terms of the current basis set. These constants are given in Table III.

The collocation method provides a relatively simple prescription for evaluating the eigenvalues and the eigenvectors of the Hamiltonian for the Ar–H_2O complex:

(1) Form a basis set as a series expansion of functions, constrained to transform as irreducible representations of the permutation-inversion (PI) group of the cluster. For atom–molecule clusters containing a light hydride, such as Ar–H_2O, the basis set given in Eq. (15) provides a good zeroth order description of the intermolecular dynamics:

$$\Psi^{J,\Gamma}(\alpha,\beta,\gamma,R,\theta,\phi)=\frac{1}{R}\sum_{\xi=0}^{1}\sum_{\epsilon=0}^{1}\sum_{\Omega=\epsilon}^{J}\sum_{j=\Omega}^{j^{\max}}\sum_{k=0}^{k^{\max}}\sum_{n=1}^{N^R}C_{\xi\epsilon\Omega jkn}\chi_n(R)\times(1+\delta_{0\Omega})^{-1/2}\{D^{J*}_{M\Omega}(\alpha,\beta,0)S^{j\xi*}_{\Omega k}(\gamma,\theta,\phi)+(-1)^{\epsilon}D^{J*}_{M-\Omega}(\alpha,\beta,0)S^{j\xi*}_{-\Omega k}(\gamma,\theta,\phi)\}. \tag{15}$$

Here $\epsilon=0$ when $J=0$. The function

$$S^{j\xi*}_{\Omega k}(\gamma,\theta,\phi)=(1+\delta_{0k})^{-1/2}\{D^{j*}_{\Omega k}(\gamma,\theta,\phi)+(-1)^{\xi}D^{j*}_{\Omega -k}(\gamma,\theta,\phi)\},$$

is a standard Wang transformation of the symmetric top basis functions. The $D^{j*}_{\Omega k}(\gamma,\theta,\phi)$ functions are normalized Wigner D matrices in the phase convention of Condon and Shortley. The functions $\chi_n(R)$ are chosen to be any suitable radial basis set which spans the space of the relevant intermolecular dynamics. The size of the basis set is determined by the number of radial functions (N^R), the number of functions with different values of j (N^θ) (note that $j^{\max}$ is not equal to $N^\theta-1$ for all matrices since $j^{\min}$ is not necessarily equal to zero), and the maximum value of k included ($k^{\max}$). For Ar–H_2O, there are four irreducible representations in the molecular symmetry group $C_{2v}(m)$. To reduce the computational effort, the wave functions are partitioned according to these symmetries. The Hamiltonian does not couple wave functions of different permutation-inversion symmetry at any level of approximation. The symmetrized wave functions are classified by the irreducible representations of $C_{2v}(m)$, which transform as follows:

$A_1\rightarrow k=\text{even},\quad J+\epsilon+\xi=\text{even},$

$A_2\rightarrow k=\text{even},\quad J+\epsilon+\xi=\text{odd},$

$B_1\rightarrow k=\text{odd},\quad J+\epsilon+\xi=\text{even},$

$B_2\rightarrow k=\text{odd},\quad J+\epsilon+\xi=\text{odd}.$

(2) Operate on this wave function with the Hamiltonian. This step produces a set of coupled differential equations in the 6-dimensional space, $R,\theta,\phi,\alpha,\beta,\gamma$. In the calculations described below we factor out those portions of the Hamiltonian operator which act as raising or lowering operators on the quantum number Ω. The effect of this operator (the Coriolis operator) is evaluated subsequently by direct integration over a small subset of the VRT wave functions obtained using the collocation method. This approximation reduces the size of the matrices which must be stored in core with no significant effect on the accuracy of the eigenvalues. This is equivalent to performing the calculation within the "helicity decoupling" approximation (assuming that Ω is a good quantum number) and then recoupling these approximate solutions to obtain the exact result.

(3) Left multiply by a parity adapted spatial rotational wave function such as

$$R(1+\delta'_{0\Omega})^{-1/2}\{D^{J*}_{M\Omega'}(\alpha,\beta,0)e^{i\Omega'\gamma} + (-1)^{\epsilon'+\Omega'}D^{J*}_{M-\Omega'}(\alpha,\beta,0)e^{-i\Omega'\gamma}\}, \quad (16)$$

and integrate over the angles which are arguments of the spatial wave function (in this case α,β,γ) to eliminate the dependence of the coupled differential equations created in Step 2 on the spatial orientation of the cluster. We also include the factor of R in Eq. (16) to simplify the resulting coupled differential equations, but this is not necessary.

(4) Choose a set of collocation points $[R_{n'},\theta_{j'k'},\phi_{j'k'}]_{\epsilon'\Omega'}$ and evaluate the modified coupled differential equations created in Step 3 on this set of points. This step arranges the coupled differential equations in the form of a generalized unsymmetric eigenvalue problem. The rows of this matrix equation are labeled by the collocation points and the columns are labeled by the corresponding basis function. If the IPS has symmetry, it is advantageous to restrict the points chosen to be from the smallest region of the potential which is mapped onto the full IPS by successive symmetry operations. This is analogous to recognizing that an integral over a symmetric function may be performed over the full range of the integration or it may be performed only over the unique region and then multiplied by a constant describing the symmetry. In the application of the collocation method this extra constant becomes incorporated into the eigenvector matrix.

(5) Solve the unsymmetric matrix eigenvalue problem, usually with a standard library routine.

The solutions to the unsymmetric eigenvalue problem can, in principle, be complex and have nonorthogonal eigenvectors. However, Yang and Peet[48] have shown that the collocation method is an approximation to the variational solutions to the Schrödinger equation with the same accuracy as would be obtained if the integrals were evaluated by Gaussian quadrature on the collocation points. In our own experience, when a sufficient number of functions/points are used, the complex components of the eigenvalues are observed to approach zero and the eigenvectors obtained are orthogonal to a high level of precision.

The most significant changes from our previous application of this method are the use of contracted radial functions and improved distribution of the angular points. The use of contracted radial functions was discussed by Peet and Yang[47] in their application of the collocation method to the study of Ar–HCl. For our purposes, contracted radial functions have the advantage of more uniform convergence of states with two quanta of stretching excitation than methods which simply limit the range over which functions are placed, as we described in Ref. 13. We find that all of the states required to determine the IPS are converged to 0.01 cm^{-1} when using nine contracted radial functions. Approximate radial eigenfunctions are obtained by solving a one-dimensional problem on a radial potential surface which represents the distance of closest approach at the dissociation energy ($R_{E=0}$) of the two subunits on the multidimensional surface and the well depth at the absolute minimum ($\epsilon_{\min}$) on that surface. These parameters are chosen such that the eigenvectors of the one-dimensional Hamiltonian span the radial space of the full three-dimensional IPS. One potential which meets these criteria was proposed by Peet and Yang

$$V(R)=4\epsilon_{\min}\left[\left(\frac{R_{E=0}}{R}\right)^{12}-\left(\frac{R_{E=0}}{R}\right)^{6}\right]. \quad (17)$$

However, this potential can not simultaneously represent the distance of closest approach and the position of the radial minimum on the true $Ar–H_2O$ surface very well (although it does for other potentials). As a result, each eigenvector on the three-dimensional surface has substantial contributions from several eigenvectors of the one-dimensional surface. This is does not present any computational difficulties, but it makes interpretation of the eigenvectors somewhat more difficult than necessary. The model potential

$$V(R)=Ae^{-\beta(R-R_{\rm ref})}-\sum_{n=6}^{8}C_nD_n(R)R^{-n}, \quad (18)$$

with $A=215$ cm^{-1}, $\beta=2.30$ $Å^{-1}$, $R_{\rm Ref}=3.6$ Å, $C_6=53.91$ hartree $(a_0)^6$, $C_7=1155$ hartree $(a_0)^7$, and $C_8=3015$ hartree $(a_0)^8$ was used instead. The potential constants A, β, and C_7 and C_8 were adjusted to give approximately $R_{E=0}\approx 2.95$ Å, $\epsilon_{\min}\approx 160$ cm^{-1}, and $R_{\min}\approx 3.6$ Å, (the position of the radial minimum on the full three-dimensional surface). This choice of $R_{E=0}$ and $\epsilon_{\min}$ insured that the contracted wave functions would span the entire space of the intermolecular dynamics in the radial coordinate throughout the least squares fits. C_6 was fixed at the same value used in the full three-dimensional calculation, 53.91 hartree $(a_0)^6$, and the other values were chosen somewhat arbitrarily. The first few contracted functions on this one-dimensional surface closely mimic the fully coupled radial eigenfunctions, making it easier to interpret a list of the eigenvectors. Convergence of the full three-dimensional eigenvalues may also be slightly faster using the improved model one-dimensional potential, but not significantly. For both potentials, the contracted functions were generated by distributing 40 Gaussian functions evenly between 2.8 and 5.9 Å, and solving the one-dimensional Hamiltonian

$$H_{1D}=\frac{-\hbar^2}{2\mu}\frac{d^2}{dR^2}+V(R) \quad (19)$$

variationally. The integrals were evaluated numerically using the trapezoid rule with limits of integration well beyond the centers of the last distributed Gaussian functions. As noted by Peet and Yang,[47] and earlier by LeRoy *et al.*,[51] it is counterproductive to attempt to obtain highly accurate eigenvalues and eigenvectors for the model problem. It is preferable for the higher functions in the trial basis set to have increasing oscillation in the well, rather than the smoothly varying behavior of the eigenfunctions of the one-dimensional surface near dissociation. The one-dimensional functions with increasing oscillation in the well have more flexibility in the regions where the one-

dimensional and three-dimensional potentials are very different than would exact eigenfunctions of the one-dimensional Hamiltonian.

The second significant change in our computational approach is in the choice of points in the angular coordinates. Points in θ and ϕ must be chosen by some method which couples the two coordinates, since (1) the wave functions used are not direct-product wave functions, and (2) we choose to formulate the problem as a square matrix rather than as a rectangular problem which has more points than functions. Choosing points appropriate to these compound functions is not as obvious as for direct product functions. For an unsymmetrized set of spherical harmonics, including all $(l+1)^2$ functions from Y_{00} through Y_{ll}, Friesner[52] has described a set of collocation points which are Gauss–Legendre points in θ and evenly spaced (Gauss–Chebyshev) in ϕ. However, when symmetry is used to partition the basis set, the points must also be partitioned to obtain the optimum accuracy in the eigenvalues. We assign angular points separately for each symmetry subblock of the Hamiltonian, and within that subblock, we assign them separately for each distinct value of the pair of quantum numbers ϵ and Ω. In Ref. 4, we took the points in θ to be Gauss–Legendre points of the order of the number of distinct values of j, $(j_{\max}-j_{\min}+1)$ included in the basis. These points were taken to be an ordered set with θ_1 the Gauss–Legendre point closest to $\theta=0$ and $\theta_{N\theta}$ the Gauss–Legendre point closest to $\theta=180°$. Points in ϕ were chosen on the interval $\phi=0°$–$90°$ for each set of functions defined by a given value of j, and to be at the extrema of the highest order function in ϕ associated with the set of functions defined by that value of j. For example, for the $j=2$ function, in a B_2 symmetry $J=0$ calculation, two points in ϕ would be chosen at the extrema of the $k=2$ internal rotor basis function $(\cos 2\phi)$. Similarly, two points in ϕ would be chosen for $j=3$, but three points would be chosen for $j=4$. Since the Wigner D matrices are a nondirect product basis, the direct product of these points would give more than one point per function. A procedure for associating the points in θ and ϕ was established, such that a one-to-one correspondence in the number of functions and points is obtained. However, we have found that this procedure is inadequate when extended to potentials with higher order anisotropy than we present in the AW1 IPS.

Our new algorithm for choosing points is as follows: As before, we find points separately for each subblock of the Hamiltonian matrix and for each pair of ϵ and Ω separately within that subblock. The individual points in θ are chosen exactly as before; they are taken to be the Gauss–Legendre points of order N^θ. In ϕ we choose points on the interval 0°–90° at the extrema of the highest order function (largest value of k) in the portion of the subblock being considered. This is equivalent to choosing Gauss–Chebyshev points of order $k_{\max}$ shifted to account for the relative phase (sin vs cos) difference of the wave functions of different symmetry. We make the *association* of points in θ and ϕ with each other differently than we did previously. The points in ϕ are associated with points in θ to give the most even distribution on the surface of the unit sphere that is possible. If an exactly even distribution is not possible, then the extra functions are associated with points in θ near the potential minimum. For $Ar–H_2O$, they are distributed evenly about $\theta=90°$. Specific θ, ϕ associations proceed in order. For example, if five points are chosen in ϕ the ordering proceeds as follows: (θ_1,ϕ_1), (θ_1,ϕ_2), (θ_1,ϕ_3), (θ_2,ϕ_4), (θ_2,ϕ_5), (θ_2,ϕ_1), (θ_3,ϕ_2), etc. It is worth noting that this new procedure does not ever require the implicit association of a given point in the configuration space of the problem with a particular function, in contrast to our previous method. This new algorithm gives stable uniform convergence for all four of the different C_{2v} symmetry blocks.

TABLE IV. Convergence of the collocation method. Energies of the $J=0$ A_1 and B_2 eigenstates with the basis sets of 9/10/8, 15/10/8, 9/12/11, and 13/12/11 as defined in the text.

9/10/8	15/10/8	9/12/11	13/12/11
A_1			
−98.329 527	−98.333 004	−98.328 544	−98.332 450
−68.082 548	−68.066 903	−68.076 708	−68.060 282
−57.650 341	−57.674 869	−57.650 484	−57.677 107
−39.252 497	−39.223 823	−39.250 009	−39.218 704
−32.858 275	−32.863 308	−32.840 428	−32.845 988
−27.130 360	−27.217 933	−27.125 563	−27.212 643
−18.177 299	−18.108 819	−18.176 983	−18.267 676
−8.715 959	−8.115 251	−8.717 035	−13.360 211
B_2			
−81.582 494	−81.585 959	−81.580 304	−81.584 198
−47.608 308	−47.584 628	−47.607 623	−47.584 679
−25.006 934	−25.016 082	−24.993 721	−24.997 745
−15.981 081	−15.951 227	−15.973 842	−15.948 887
−0.611 178	−0.662 878	−0.610 803	−0.655 204
10.425 754	10.334 113	10.432 839	8.836 263
16.413 267	17.368 084	16.420 200	12.233 347
24.227 976	26.767 243	24.228 206	19.652 251

The convergence of the calculations with respect to the number of functions/points follows the general pattern established by Peet and Yang in calculations of Ar–HCl eigenvalues,[47] and which we described in Ref. 4 with respect to $Ar–H_2O$. The number of functions needed to obtain reliable energies for the least squares fits is somewhat larger than in our previous calculations because of the presence of higher order anisotropies in the new IPS, a substantial decrease in the binding energy (20%), and the need to obtain accurate eigenvalues for states which are near to the dissociation threshhold. We choose a basis/point set of size $N^R=9$, $N^\theta=10$, and $k_{\max}=8$ (denoted 9/10/8 for simplicity) and use a radial interval from $R_{\min}=2.9$ Å to $R_{\max}=5.9$ Å. In Table IV we list A_1 and B_2 $J=0$ eigenvalues obtained using this basis set and the larger basis sets—15/10/8, 9/12/11, and 13/12/11. It is evident that the lowest eigenvalues are converged to 0.01 cm^{-1} using the 9/10/8 basis. We estimate convergence of the VRT energy differences using this basis to be better than 750 MHz. Most $J=1\leftarrow0$ rotational transitions are converged to better than 5 MHz (the experimental precision is typically ~1 MHz). Uncertainties in computed

$J=2\leftarrow 1$ transition energies are roughly twice those of the $J=1\leftarrow 0$ transitions. For states affected by strong Coriolis mixing, the uncertainty in l-type splittings and rotational energy differences can be much larger because of the uncertainty in the spacing of the associated VRT state origins. Estimates of these uncertainties were made using the approximate formulas for the Coriolis splittings derived in Ref. 16. These data were weighted accordingly in the fits. This 9/10/8 basis set gives matrices of dimensions 270, 252, 252, and 252 for the A_1, A_2, B_1, and B_2 $J=0$, $\Omega=0$ blocks of the Hamiltonian, respectively. Matrices for $\Omega>0$ are about two times larger.

A few other comments about convergence are in order, since it is possible that the degree of convergence may change during the course of the least squares fits. We find that the convergence of the radial basis is quite stable to large changes in the potential parameters, provided that the relevant range of the intermolecular dynamics is represented by the contracted radial basis. The distance of closest approach and the maximum extension of the radial eigenfunctions must be accessed by the contracted functions. During the course of the least squares fits described herein, there were relatively small changes in these aspects of the IPS, although the orientation at the closest approach underwent many variations. Employing a larger estimate for the well depth, a shorter distance of closest approach, and a longer $R_{\max}$ than can reasonably be expected to occur during the course of the least squares fits should provide stable convergence throughout the process. The angular basis is more difficult to deal with. Inclusion of higher order anisotropies in the well depth expansion or in the expansion of the reference distance can dramatically affect the number of angular functions that are necessary for convergence. The terms $R_m^{\lambda\mu}$ effectively generate higher order well depth anisotropies at distances away from the potential minimum. This can be seen by examining the form of the C_8 and C_9 coefficients as defined in Eqs. (9) and(10). If $R_m^{\lambda\mu}$ and $\beta_{\lambda\mu}$ were isotropic, then these dispersion coefficients would have the form of the nonzero spherical harmonic expansion coefficients ($\epsilon_{\lambda\mu}$) at all distances. Multiplication of $\epsilon_{\lambda\mu}$ by anisotropic terms in these two expansions in Eqs. (9) and (10) causes C_8 and C_9 to be proportional to additional higher order spherical harmonic terms. Since for the purposes of the least squares fits we place a premium on using the smallest basis set of sufficient accuracy, for large changes in any of these parameters, we found it necessary to confirm that the eigenvalues were adequately converged.

Isotopomers

Calculations of the VRT spectra of isotopomers of Ar–H_2O proceed in an identical fashion. In principle, each different monomer vibrational level of each isotopomer represents a different average geometry, and hence separate IPS represent the intermolecular forces for each case. We choose to represent all of these different potentials in a coordinate system referenced to an origin at the center of mass of the ground state (R_0) structure of the $H_2{}^{16}O$ isotope. All of the calculations, however, proceed with R', θ', and ϕ' defined relative to the center of mass of the monomer in question. For the symmetric isotopomers, no other changes in the computational methods are necessary. For Ar–HDO there is less symmetry and the calculations must be performed using a basis set which is twice as large as the one for the H_2O and D_2O isotopes. Since there is only one Ar–HDO VRT band available at this time we have not incorporated these data. The $H_2{}^{16}O$, $H_2{}^{17}O$, and D_2O rotational constants, the center of mass distances relative to the oxygen atom, and the reduced masses are listed in Table III. In the calculation of $H_2{}^{17}O$ properties we fix the quartic centrifugal distortion constants to those of the normal isotope. As can be seen from Table III, the rotational constants of the $H_2{}^{16}O$ and the $H_2{}^{17}O$ isotopes are nearly identical. This approximation is thus not expected to affect the accuracy of any of the calculated properties of the Ar–$H_2{}^{17}O$ isotopomer.

Eigenvectors: Dipole moments, quadrupole hyperfine structure, and the Coriolis operator

The eigenvectors of the Hamiltonian are routinely obtained from the collocation calculations. They are expressed as coefficients describing a linear combination of the basis set used. For example (Table V), we present the square modulus of the eigenvectors of selected $J=2$ states for Ar–H_2O calculated on the AW2 IPS. The coefficients describe a linear combination of basis set defined in Eq. (15). These eigenvectors demonstrate clearly that angular–radial coupling has little effect on the ortho $n=0$, $j=1$ states. The square modulus of the eigenvectors of each of these states is nearly 90% the $n=0$ contracted function. The ground state radial wave function of the complex is given approximately by the following linear combination of contracted functions: [0.96 $n=0-0.23$ $n=1$]. The square modulus of this eigenvector accounts for most of the ortho $n=0$ radial eigenfunctions, and for the eigenfunctions of $\Sigma(0_{00})$, $\Pi(1_{11})$, and $\Pi(2_{12})$. The $n=1$ ortho eigenfunctions are also dominated by a single component function of the primitive basis, evidence that there is comparatively little angular–radial coupling affecting even these excited stretching states. However, in the $\Sigma(1_{11})$ para state, the $n=0$ eigenfunction accounts for less than 60% of the square modulus of the total eigenvector. The coefficients of the eigenvector for this state may be compared with those of the less strongly mixed ortho $n=0$ and $n=1$ states to show that the $\Sigma(1_{11})$ state is mixed primarily with $n=1$, $\Sigma(0_{00})$ but also with $n=2$, $\Sigma(0_{00})$. The $\Sigma(2_{12})$ state is also strongly mixed. The full three-dimensional eigenfunction is close to a 50:50 mixture of $\Sigma(2_{12})$ and $n=2$, $\Sigma(1_{01})$. This is much stronger than the mixing of $\Pi(2_{12})$ with $n=2$, $\Pi(1_{01})$, presumably because the latter two states are not as close in energy in the absence of angular–radial coupling. These Π states are also less strongly mixed because they sample out-of-plane geometries for which the angular radial coupling is smaller (see Figs. 1 and 2).

TABLE V. Square modulus of the wave functions for the lowest few states $J=2$ states of Ar–H_2O. Only components with contributions greater than 0.01 are shown. n is an index referring to the orthonormal contracted radial basis function, and the labels on the Wang symmetrized function $S^{J,\epsilon^*}_{\Omega,k}$ are as defined by Eq. (15). We use the same letter S to designate the angular component of the wave function, but refer here to the total end-over-end rotational and angular wave function. The wave functions are normalized such that the sum of the square of the coefficients of the orthonormal basis states is equal to one. These eigenvectors were calculated on the AW2 IPS described below.

Assignment	$\lvert\Psi\rvert^2$
$\Sigma(0_{00})$	$[0.91n=0+0.05n=1]S^{0,0*}_{0,0}+[0.02n=0]S^{2,0*}_{0,2}$
$n=1,\Sigma(0_{00})$	$[0.03n=0+0.55n=1+0.05n=2]S^{0,0*}_{0,0}+[0.33n=0+0.02n=1]S^{1,0*}_{0,0}$
$\Pi(1_{11})$	$[0.89n=0+0.05n=1]S^{1,0*}_{1,0}+[0.03n=0]S^{2,1*}_{1,2}$
$\Sigma(1_{11})$	$[0.23n=1+0.14n=2]S^{0,0*}_{0,0}+[0.57n=0+0.02n=1+0.02n=2]S^{1,0*}_{0,0}$
$n=2,\Sigma(0_{00})$	$[0.07n=1+0.55n=2+0.19n=3]S^{0,0*}_{0,0}+[0.01n=0+0.13n=1]S^{1,0*}_{0,0}$
$\Sigma(1_{01})$	$[0.94n=0+0.04n=1]S^{1,1*}_{0,1}$
$\Pi(1_{01})$	$[0.88n=0+0.07n=1]S^{1,1*}_{1,1}+[0.01n=0+0.02n=1]S^{1,0*}_{1,1}$
$\Pi(1_{10})$	$[0.03n=0+0.02n=1]S^{1,1*}_{1,1}+[0.89n=0+0.02n=1]S^{1,0*}_{1,1}+[0.01n=0]S^{2,1*}_{1,1}$
$n=1,\Sigma(1_{01})$	$[0.02n=0+0.82n=1+0.06n=2]S^{1,1*}_{0,1}+[0.06n=0]S^{2,1*}_{0,1}$
$\Sigma(1_{10})$	$[0.91n=0+0.08n=1]S^{1,0*}_{0,1}$
$n=1,\Pi(1_{01})$	$[0.04n=0+0.69n=1+0.18n=2]S^{1,1*}_{1,1}+[0.02n=0+0.03n=2]S^{1,0*}_{1,1}+[0.03n=0]S^{2,1*}_{1,1}$
$n=1,\Pi(1_{10})$	$[0.04n=1+0.03n=2]S^{1,1*}_{1,1}+[0.01n=0+0.80n=1+0.08n=2]S^{1,0*}_{1,1}$
$\Sigma(2_{12})$	$[0.39n=2+0.02n=3]S^{1,1*}_{0,1}+[0.54n=0+0.01n=1]S^{2,1*}_{0,1}+[0.02n=0]S^{2,1*}_{1,1}$
$\Pi(2_{12})$	$[0.02n=2]S^{1,1*}_{0,1}+[0.07n=2]S^{1,1*}_{1,1}+[0.01n=0]S^{1,0*}_{1,1}+[0.82n=0+0.04n=1]S^{2,1*}_{1,1}$
$n=2,\Sigma(1_{01})$	$[0.07n=1+0.35n=2+0.16n=3]S^{1,1*}_{0,1}+[0.32n=0+0.07n=2]S^{2,1*}_{0,1}$
$\Delta(2_{12})$	$[0.89n=0+0.07n=1]S^{2,1*}_{2,1}$

In addition to allowing the assignment of the eigenvalues, the wave functions can, of course, be used to calculate any properties of interest, such as $\langle\cos\theta\rangle$, $\langle R\rangle$ or $\langle R^2\rangle$. Two properties are of special interest for predicting near and far infrared VRT spectra and for testing the accuracy of the IPS, viz., the transition moment and the nuclear quadrupole hyperfine coupling constants. Expressions for the operators describing these properties have been given by Hutson.[21] The z component of the space-fixed dipole moment operator is given by

$$\mu_z=\left[\mu_{H_2O}+\frac{2\mu_{H_2O}\alpha_{Ar}}{R^3}\right]\sum_{\Omega} D^{1*}_{0\Omega}(\alpha,\beta,0)\,D^{1*}_{\Omega k}(\phi,\theta,\gamma), \tag{20}$$

where we include the contribution of the dipole–induced dipole, but neglect the contribution of higher order permanent moments (quadrupole, octupole, $\cdots$) to the induced dipole, and the script D's indicate Wigner D matrices which have not been normalized. For FIR VRT bands of Ar–H_2O, which acquire intensity from the pure rotational transitions of the monomer, $k=0$. Infrared transitions to the asymmetric stretching vibration of water involve the matrix elements of $k=+1$ and $k=-1$. Matrix elements of this operator between the primitive functions

$$D^{J*}_{M\Omega}(\alpha,\beta,0)\,D^{j*}_{\Omega k}(\phi,\theta,\gamma),$$

which are the angular portion of the basis set defined in Eq. (17), have been given by Hutson[21]

$$\left[\mu_{H_2O}+\frac{2\mu_{H_2O}\alpha_{Ar}}{R^3}\right]\sum_{\Omega}(-1)^{M_i-\Omega_i}[(2j_i+1)\times(2j_f+1)(2J_i+1)(2J_f+1)]^{1/2}\times\begin{pmatrix} j_1 & 1 & j_f\\ -k_i & k & k_f\end{pmatrix}\begin{pmatrix} j_i & 1 & j_f\\ -\Omega_i & 0 & \Omega_f\end{pmatrix}\times\begin{pmatrix} J_i & 1 & J_f\\ -\Omega_i & 0 & \Omega_f\end{pmatrix}\begin{pmatrix} J_i & 1 & J_f\\ -M_i & 0 & M_f\end{pmatrix}. \tag{21}$$

In Eq. (21), we represent the transition moment matrix element in a standard bra, ket notation, where i labels the initial state vector and f the final state vector. In our calculations we have evaluated the transition matrix elements ($\langle f|\mu|i\rangle$) between the eigenfunctions of the three-dimensional Hamiltonian by combining the analytical form of the angular matrix elements [Eq. (21)] and numerical integration over the radial coordinate. The $J=1\leftarrow J=0$, $M_J=0\leftarrow 0$ transition matrix elements computed in this manner were then scaled by a factor of $\sqrt{3}$ as described by Fraser *et al.*[25] to express them as a transition dipole moment in Debye.

The quadrupole coupling constants of Ar–$H_2{}^{17}O$ or Ar–D_2O are expectation values of the operators Q_{20} and Q_{22}

$$Q_{20}=q_{20}D^{2*}_{00}(\phi,\theta,\gamma)+q_{22}[D^{2*}_{02}(\phi,\theta,\gamma)+D^{2*}_{0-2}(\phi,\theta,\gamma)], \quad (22)$$

$$Q_{22}=q_{20}D^{2*}_{20}(\phi,\theta,\gamma)+q_{22}[D^{2*}_{22}(\phi,\theta,\gamma) + D^{2*}_{2-2}(\phi,\theta,\gamma)], \quad (23)$$

where $q_{20}=q_{bb}$ and $q_{22}=1/\sqrt{6}(q_{aa}-q_{cc})$, in terms of the quadrupole coupling constants (q_{xx}) of the monomer, which are listed in Table III. These operators are diagonal in J. Expectation values of Q_{20} and Q_{22} are easily evaluated by an analytic sum over the component wave functions, by analogy to Eq. (21) (see also Hutson[21]) and the 1 in the first two 3-j symbols replaced by 2, omitting the second two 3-j symbols, and substituting the appropriate quadrupole constants for the dipole and induced dipole moments. The experimental observables eQq_{aa} and $[eQq_{bb}- eQq_{cc}]$ are given by the relations $eQq_{aa}=Q_{20}$ and $[eQq_{bb}- eQq_{cc}] =2Q_{22}$. However, observed spectra do not always allow these two components to be separated. We neglect contributions from induction to the quadrupole hyperfine structure of the complex, since these are much smaller than the induction contributions to the transition moment. As a result, the expectation value of these operators is diagonal in the radial basis set. For ease of computation, the Ar–$H_2{}^{17}O$ nuclear quadrupole coupling constants are computed using the Ar–$H_2{}^{16}O$ wave functions. This approximation is expected to be accurate to about 1%, using the ratio of $H_2{}^{16}O$ to $H_2{}^{17}O$ rotation constants as a guide. It should also be pointed out that Coriolis effects on the quadrupole structure of many states will be at a level of 1% or greater.

In Table VI, we present the $J=0$ and $J=1$ eigenvalues of Ar–H_2O and of Ar–D_2O from the AW2 IPS, which is described below. The identifying labels used for each state represent the dominant contributions to the VRT wave function. These eigenvalues are calculated employing a 9/10/8 basis with $R_{\min}=2.9$ and $R_{\max}=5.9$ Å. This basis set is adequate to converge all of the levels shown, except those assigned to $n=3$, to better than 0.1 cm^{-1}. We also present in this table the transition moments for transitions from $J=0$ in the para $[\Sigma(0_{00})]$ and ortho $[\Sigma(1_{01})]$ ground states to all of the $J=1$ states connected by electric dipole selection rules, and the expectation values of Q_{20} and Q_{22} for Ar–$H_2{}^{17}O$ and Ar–D_2O.

Our last use of the eigenvectors is to evaluate the Coriolis matrix elements. Individual subblocks of the collocation matrix with distinct values of Ω are evaluated separately, increasing the speed of the overall computation significantly. The off-diagonal portion of the rotational operator which couples eigenstates defined by the primitive basis is then evaluated by a combination of analytic and numerical integration using the wave functions obtained in the original collocation solution. We retain the eight lowest energy states of each Ω and create a small matrix with diagonal elements the energies obtained by collocation and off-diagonal elements the Coriolis coupling matrix elements. The resulting eigenvalues are negligibly different from those obtained by direct evaluation of the full matrix by collocation. For high J states, we include only those Ω subblocks which are necessary to describe the eigenvalues and eigenvectors of the states of interest. Typically this would include only $\Omega=0,1$, and 2. In some cases, e.g., the $J=2$ A_1 states included in the least squares fits, it is adequate to omit $\Omega=2$ as well.

LEAST SQUARES FITS

The process of improving on the AW1 Ar–H_2O IPS began with fits of the data involving $J=0$ and $J=1$ term values for the normal isotope. Initial iterations generated an improved surface with Ar–H_2O data alone, then fits were performed using the combined set of Ar–H_2O and Ar–D_2O energy differences, the absolute value of the dipole moment of the Ar–H_2O $\Sigma(0_{00})$ state, and the ^{17}O nuclear quadrupole coupling constants in $\Sigma(0_{00})$ and $\Sigma(1_{01})$ given in Table I. The data included in the fits were weighted by the inverse square of the larger of the estimated computational, model or experimental uncertainty. The relative weights used are similar to those employed in the fits used to derive the AW1 surface,[4] but the absolute weights are about a factor of 2 larger, reflecting the slower convergence of the calculations. The uncertainties and the residuals for observables calculated on the AW2 IPS are shown in Table I.

In the early stages of these fits, and with the use of a small basis set, we explored whether the parameter set used to describe the AW1 surface was sufficient to describe the newly available data, and attempted to ascertain which new parameters are required to fit this data. A few iterations of the least squares loop were run with some of the parameters held constant and others allowed to vary. Not surprisingly, the larger angular–radial coupling evident in the vibrational energies of $\Sigma(1_{11})$, $\Sigma(2_{12})$, and $\Pi(2_{12})$, in the l-type splitting in $\Pi(1_{11})$ and $\Pi(2_{12})$, and the $J=1\leftarrow 0$ rotational term value in $\Sigma(1_{11})$ required inclusion of higher order terms in the expansion $R_m^{\lambda\mu}$ than were used in the AW1 surface. Both R_m^{30} and R_m^{32} have been included to more accurately reflect the shape of the H_2O molecule in and out of the molecular plane. However, the values of these two parameters are highly correlated (0.96) and a nearly equivalent fit could be obtained by fixing R_m^{30} at zero. In the monomer plane, both of these parameters increase the van der Waals bond length at the hydrogen bonded orientation and decrease it at approaches along the OH bond vector from the oxygen side. The difference is that R_m^{30} has the same effect both in and out of the monomer plane, while R_m^{32} has a dependence on the angle ϕ and can contribute to structure in the IPS both near the hydrogens and near the lone pairs on the oxygen. These terms also allow closer approach of the argon in the space between the hydrogen atoms. On the AW1 surface, since they were constrained to be zero, the repulsive forces in between the hydrogen atoms are too large to allow the argon to approach any closer than it does directly along the OH bond. Similarly, the AW1 parameters did not allow any structure in the IPS which might reflect the presence of

TABLE VI. The calculated $J=0$, and 1 eigenvalues, the transition moments for allowed $J=1\leftarrow 0$ transition originating in the lowest ortho $[n=0,\Sigma(1_{01})]$ or para $[n=0,\Sigma(0_{00})]$ states, and the quadrupole hyperfine coupling constants for Ar–H_2O (MHz) and Ar–D_2O (kHz) computed on the AW2 surface. The quadrupole hyperfine constants for $J=1$ Ar–H_2O are calculated using the $H_2{}^{17}O$ hyperfine constants but the Ar–$H_2{}^{16}O$ wave functions.

Ar–H_2O		Assignment	$\lvert\langle\lvert\mu\rvert\rangle\rvert^2$	Q_{20}	Q_{22}
$J=0$ A_1	$J=1$ A_2				
−98.329 52	−98.130 12	$n=0\Sigma(0_{00})$	0.008 89	−1.23	0.00
−68.082 55	−67.893 23	$n=1\Sigma(0_{00})$	0.577 8	−1.05	0.00
	−61.293 09	$n=0\Pi(1_{11})$	2.75	−1.77	2.45
−57.650 34	−57.451 07	$n=0\Sigma(1_{11})$	0.527	−0.74	0.00
−39.252 49	−39.084 09	$n=2\Sigma(0_{00})$	0.019 9	−0.83	0.00
	−33.091 21	$n=0\Sigma/\Pi(2_{02})$	0.000 00	−2.24	2.13
−32.858 26	−32.245 81	$n=0\Sigma/\Pi(2_{02})$	0.003 86	−2.24	2.03
−27.130 36	−26.983 92	$n=1\Sigma(1_{11})$	0.000 31	−0.66	0.02
	−24.481 03	$n=1\Pi(1_{11})$	0.001 42	−1.18	2.41
−18.177 30	−18.032 76	$n=3\Sigma(0_{00})$	0.002 03	−0.51	0.00
$J=0$ A_2	$J=1$ A_1				
	−61.284 81	$n=0\Pi(1_{11})$		−1.77	2.46
	−32.673 56	$n=0\Pi(2_{02})$		−2.01	−4.17
	−24.506 95	$n=1\Pi(1_{11})$		−1.19	2.43
$J=0$ B_2	$J=1$ B_1				
−81.582 49	−81.388 10	$n=0\Sigma(1_{01})$	0.004 43	−4.03	0.00
	−70.031 298	$n=0\Pi(1_{01})$	0.054 1	0.94	5.55
	−60.306 62	$n=0\Pi(1_{10})$	2.17	−2.63	5.83
−47.608 31	−47.426 59	$n=1\Sigma(1_{01})$	0.082 5	−3.90	0.00
	−36.705 52	$n=1\Pi(1_{01})$	0.131	0.84	5.42
	−25.800 51	$n=1\Pi(1_{10})$	0.005 59	−2.31	5.87
−25.006 93	−24.854 16	$n=0\Sigma(2_{12})$	0.518	−3.40	0.04
	−20.200 37	$n=0\Pi(2_{12})$	0.732	−1.23	5.12
−15.981 08	−15.802 66	$n=2\Sigma(1_{01})$	0.195	−3.54	0.02
	−10.511 01	$n=2\Pi(1_{01})$	0.013 8	0.95	5.42
−0.611 18	−0.467 49	$n=3\Sigma(1_{01})$	0.005 34	−3.66	0.01
	0.825 71	$n=3\Pi(1_{01})$	0.000 01	−1.98	5.89
$J=0$ B_1	$J=1$ B_2				
	−70.038 119	$n=0\Pi(1_{01})$		0.94	−5.55
	−60.311 52	$n=0\Pi(1_{10})$		−2.62	−5.83
−45.424 25	−45.222 59	$n=0\Sigma(1_{10})$		−3.50	−0.002
	−36.711 57	$n=1\Pi(1_{01})$		0.85	−5.42
	−25.804 62	$n=1\Pi(1_{10})$		−2.30	−5.87
	−20.221 93	$n=0\Pi(2_{12})$		−1.20	−5.17
−13.351 46	−13.170 120	$n=1\Sigma(1_{10})$		−3.62	−0.005
	−10.520 13	$n=2\Pi(1_{01})$		0.96	−5.43
	0.819 55	$n=3\Pi(1_{01})$		−1.97	−5.90
Ar–D_2O					
$J=0$ A_1	$J=1$ A_2				
−101.070 89	−100.884 42	$n=0\Sigma(0_{00})$	0.025 4	41.7	0.00
	−81.705 12	$n=0\Pi(1_{11})$	3.25	55.6	−63.0
−80.383 01	−80.157 22	$n=0\Sigma(1_{11})$	0.546	22.8	−1.7
−68.939 86	−68.807 37	$n=0\Sigma(2_{02})$	0.008 9	32.3	−1.5
	−66.272 06	$n=0\Pi(2_{02})$	0.006 41	39.4	−76.1
−64.839 27	−64.619 47	$n=1\Sigma(0_{00})$	0.025 4	33.2	−2.0
	−48.234 95	$n=1\Pi(1_{11})$	0.007 16	19.0	−24.0
−47.738 47	−47.521 65	$n=1\Sigma(1_{11})$	0.000 65	21.7	−1.1
	−43.467 63	$n=0\Pi(2_{11})$	0.019 7	−13.2	5.8
−40.942 51	−40.789 38	$n=2\Sigma(0_{00})$	0.000 16	23.1	−0.1
	−33.704 48	$n=1\Pi(2_{02})$	0.003 3	35.6	−30.7
−33.552 70	−32.900 21	$n=1\Sigma(2_{02})$	0.000 22	37.6	−46.7
$J=0$ A_2	$J=1$ A_1				
	−81.666 59	$n=0\Pi(1_{11})$		56.5	64.7
	−66.277 69	$n=0\Pi(2_{02})$		39.8	79.6
	−48.300 45	$n=0\Pi(2_{11})$		13.2	17.1
−48.027 96	−47.755 46	$n=1\Sigma(2_{11})$		12.1	8.5
	−43.441 16	$n=0\Pi(2_{11})$		−13.7	−16.1
	−33.224 14	$n=1\Pi(2_{02})$		40.3	77.5

TABLE VI. (*Continued.*)

Ar–D_2O		Assignment	$\lvert\langle\lvert\mu\rvert\rangle\rvert^2$	Q_{20}	Q_{22}
$J=0$ B_2	$J=1$ B_1				
−95.299 70	−95.117 76	$n=0\Sigma(1_{01})$	0.013	76.7	−0.05
	−84.207 46	$n=0\Pi(1_{01})$	0.774	12.8	−97.6
	−81.170 89	$n=0\Pi(1_{10})$	1.80	41.8	−97.0
−66.012 88	−65.848 27	$n=0\Sigma(2_{12})$	0.534	64.6	−0.33
	−59.263 61	$n=0\Pi(2_{12})$	0.638	25.4	−98.5
−57.072 53	−56.881 94	$n=1\Sigma(1_{01})$	0.137	65.8	−1.1
	−50.654 67	$n=1\Pi(1_{01})$	0.001	−7.7	−97.2
	−47.681 53	$n=1\Pi(1_{10})$	0.003	51.2	−96.8
−35.252 52	−35.125 80	$n=1\Sigma(2_{12})$	0.003	57.1	−6.7
−33.993 51	33.963 09	$n=0\Sigma(3_{03})$	0.000 1	41.3	−84.0
	−32.064 56	$n=0\Pi(3_{03})$	0.025	34.3	−84.3
$J=0$ B_1	$J=1$ B_2				
	−84.212 87	$n=0\Pi(1_{01})$		13.4	98.1
	−81.175 54	$n=0\Pi(1_{10})$		41.3	94.6
−66.763 91	−66.575 60	$n=0\Sigma(1_{10})$		−50.5	0.002
	−59.260 32	$n=0\Pi(2_{12})$		22.0	97.3
	−50.663 07	$n=1\Pi(1_{01})$		11.4	100.6
	−47.684 85	$n=1\Pi(1_{10})$		34.2	96.1
−35.234 41	−35.063 70	$n=1\Sigma(1_{10})$		−52.6	0.005
	−32.248 00	$n=0\Pi(3_{03})$		32.3	93.1

localized lone pairs by allowing closer approach at $\theta=180°$, than at $\theta=125°$ in the plane perpendicular to the H_2O monomer.

The second major change to the AW1 parameters required by the new Ar–H_2O data is the size of the isotropic well depth, (ϵ_{00}). In initial iterations of the fits, the value of this parameter plummeted from its value on the AW1 surface of 153.3(2.2) cm^{-1} to about 120 cm^{-1}, with a large increase in the highly correlated (−0.98 on the AW1 surface) parameter β_{00} from 2.501(32) $Å^{-1}$ to a final value of 3.617(48) $Å^{-1}$ on the AW2 IPS. The correlation between these two parameters is somewhat lower (−0.96) in the AW2 parameters and the uncertainty in ϵ_{00} is more than two times lower permitting much more confidence in the new value of $\epsilon_{00}=118.15(88)$. Test runs with selected data removed from the input indicate that the well depth is sensitive to the Σ and $\Pi(2_{12})$ data, although many other measurements also contribute. Most likely, it is the strong coupling of the 2_{12} states to the $n=2\Sigma$ and $\Pi(1_{01})$ levels which places experimental constraints on the isotropic well depth. The sensitivity of the 2_{12} data to ϵ_{00} and β_{00} has the unfortunate consequence of reducing the ability of these data to precisely determine the values of ϵ_{30} and ϵ_{32}. These two parameters were highly correlated (0.97) and not very well determined in nearly converged fits to the data. In the final iterations, ϵ_{32} was fixed at 0, a value not very different from that obtained when it was free to vary. Because of this arbitrary constraint, additional spectra of $j=2$ states, and measurements of the $n=2$ stretching levels would be particularly valuable as a test of the AW2 surface.

After initial runs to determine a range of parameters to vary, data for both isotopes were included as input to the least squares loop. The error introduced in requiring the two isotopes to move on a single IPS (rather than allowing each to move on a different effective IPS averaged over the high frequency motions of the monomer) is expected to depend on the OH to OD bond length difference of 0.0037 Å.[53] Some of the parameters $R_m^{\lambda\mu}$ in the final IPS are determined to this level of precision. It is possible that the accuracy of the AW2 potential is limited by the requirement that the two isotopes move on the same IPS. However, a potential of equivalent accuracy and detail cannot be extracted from separate fits to each individual isotope, and we feel it is more likely that omitting high order parameters in the three components of the potential expansion is the most severe limitation.

The final fits were performed with a basis set of 9/10/8 on the radial interval 2.9–5.9 Å. During the course of these fits R_m^{20} was found to approach zero, and to be undetermined. Accordingly, it was fixed at zero. Twelve parameters were required to reproduce the 37 VRT measure-

TABLE VII. Parameters describing the AW2 IPS defined by Eqs. (1)–(11). The uncertainties indicated in parentheses represent 2σ (95%) confidence intervals.

	AW1	AW2
β_{00} ($Å^{-1}$)=	2.501(32)	3.617(48)
ϵ_{00} (cm^{-1})=	153.3(2.2)	118.15(88)
ϵ_{10} (cm^{-1})=	1.90(24)	2.15(15)
ϵ_{20} (cm^{-1})=	4.518(72)	4.52(24)
ϵ_{22} (cm^{-1})=	19.301(54)	20.949(92)
ϵ_{30} (cm^{-1})=	0(fixed)	−6.7(1.4)
ϵ_{32} (cm^{-1})=	0(fixed)	0.(fixed)
ϵ_{40} (cm^{-1})=	0(fixed)	−1.46(42)
R_m^{00} (Å)=	3.6339(13)	3.6098(14)
R_m^{10} (Å)=	0.1005(10)	0.1050(13)
R_m^{20} (Å)=	0.0128(36)	0.(fixed)
R_m^{22} (Å)=	−0.0342(17)	−0.0442(28)
R_m^{30} (Å)=	0(fixed)	−0.013(15)
R_m^{32} (Å)=	0(fixed)	0.0630(92)
# of data	11	37
# of parameters	9	12
DSE	1.14	1.20

ments. The quality of the fit is indicated by the dimensionless standard error (DSE)[42] of 1.2 and the residuals shown in Table I. The parameters of the AW2 IPS and its predecessor AW1 are shown in Table VII. Most of the data are reproduced by the AW2 potential within the estimated uncertainty. Many of the parameters have values outside the 2σ error bars of the terms in the AW1 potential. As noted above, the largest changes were in the isotropic well depth and in the slope of the repulsive wall. The change in R_m^{00} is also related to the change in the isotropic well depth, since in the AW1 parameters, it was correlated with β_{00} and ϵ_{00} at a magnitude of 0.85. The large change in ϵ_{22} may be influenced in part by the change in well depth (the correlation was 0.55 on the AW1 surface), but also partly by the inclusion of high order terms in the well depth expansion. In contrast to these terms, which have changed by many times the least squares estimate of their uncertainty, the values of ϵ_{10} and ϵ_{20} are nearly identical (2σ and 1σ, respectively) to their values on the AW1 surface.

The parameters of the new potential are expected to be much more reliable than those of the AW1 IPS, since the correlations are lower among the leading terms and since the number of parameters in the current fits is only one third the number of VRT data. In determining the AW1 surface, we used nine parameters to fit 11 VRT measurements, compared with 12 parameters and 37 measurements used in the current AW2 fit. However, we caution that the expansions used in the AW2 potential are slowly converging and that many more parameters may be necessary in an ultimate description of the IPS. While the leading isotropic terms are much larger than any of the anisotropic terms, the anisotropic terms are all about the same size. Additional high order anisotropic terms will no doubt be necessary in a more accurate description of the Ar–H_2O IPS. It would be useful to estimate some of the high order terms required to produce a more accurate potential, rather than fix them at zero. At this time, however, we do not believe that the necessary parameters can be estimated with confidence. Also some of the correlations are still uncomfortably large. While we do not show the entire correlation matrix for reasons of space, we list below all of the correlations with magnitudes greater than 0.70: β_{00} with ϵ_{00} (-0.96), ϵ_{10} with ϵ_{30} (0.76), ϵ_{20} with R_m^{30} (0.93), ϵ_{20} with R_m^{32} (0.90), R_m^{30} with R_m^{32} (0.96), R_m^{10} with R_m^{30} (-0.72), and R_m^{10} with R_m^{32} (-0.79).

After the final potential denoted AW2 had been obtained, we attempted to ascertain whether the sign of ϵ_{10} was determined unambiguously or if this potential was merely one of a family of potentials that reproduce the experimental data equally well. We do not feel that the signs of ϵ_{30} and ϵ_{32} warrant detailed investigation until the values of these parameters are more precisely determined. However, we note again that the signs of these terms are coupled to the sign of ϵ_{10} by the measurement of the ground state transition moment. ϵ_{10} was initialized at -2.0 and held fixed for the first few iterations. All other potential parameters were initialized at their AW2 values. We were unable to obtain a fit with a DSE less than five while holding ϵ_{10} negative. We take this as convincing evidence that it is, in fact, positive.

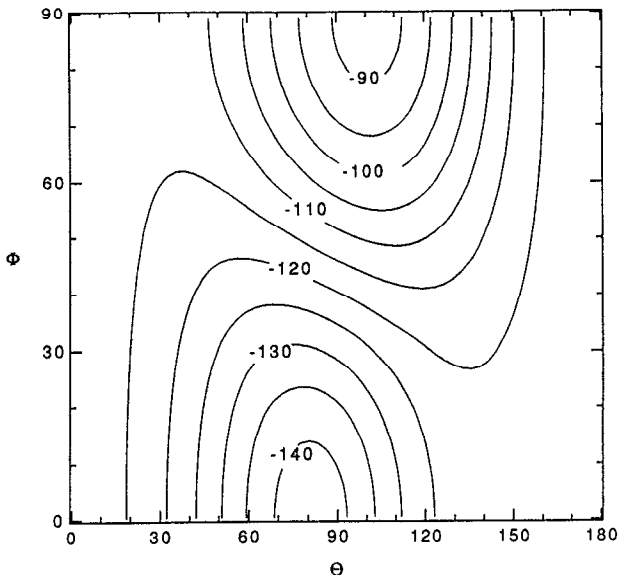

FIG. 3. The AW2 intermolecular potential surface [$R=3.6098$ Å].

The high correlation between β_{00} with ϵ_{00} remains the largest source of doubt about the accuracy of the AW2 IPS. However, there are several pieces of circumstantial evidence that lend support for values of these parameters that are at least close to the AW2 values. First, the AW2 well depth is within 15% of the well depths obtained by *ab initio* calculations.[22,23] Second, the *ab initio* estimate of the well depth by Bulski *et al.*[23] has been shown to reproduce the magnitude and temperature dependence of the second virial coefficient. Since these authors also show that the second virial coefficient is insensitive to the anisotropy in the IPS, this similarity in the well depths is sufficient to indicate that the AW2 surface will also reproduce the experimental pressure second virial coefficients. Finally, the slope of the repulsive wall on the AW2 IPS [β_{00}] is determined to be 3.617(48), close to the values of this constant in the H6(3) Ar–HCl [$\beta_{00}=3.58(18)$ $Å^{-1}$][29] and the TT_3 Ar–H_2 [$\beta_{00}=3.582(46)$ $Å^{-1}$][42] surfaces, which have similar parameterizations. This may imply that $\beta_{00}\approx 3.6$ $Å^{-1}$ is a molecular constant which is transferrable from one complex of argon with a light hydride to another. The similarity is at least suggestive that the slope of the repulsive wall on the AW2 surface is more nearly correct than that of its predecessor.

THE AW2 POTENTIAL SURFACES

The AW2 potential describes the intermolecular forces in the three-dimensional Ar–H_2O system at a level of detail and precision which has been previously attained only for the topologically simpler atom–diatom systems: Ar–HF, Ar–HCl, and the Rg–H_2 complexes.[3,7,8] Plots of the surface described by the parameters in Table VII are shown in Figs. 1–3. These show (1) the IPS in the plane of the water molecule ($\phi=0°$); (2) the IPS in the plane perpendicular to the water molecule ($\phi=90°$); and (3) the angular IPS at

$R=R_m^{00}=3.6098$ Å. These plots show that the AW2 IPS is substantially more structured than its predecessor, the AW1 surface, shown in Fig. 1 of Ref. 4. As in all recent studies of the IPS for $Ar-H_2O$,[4,21–23] the new IPS exhibits a global potential minimum for orientations with the argon located in the plane of the water monomer and with the R vector oriented nearly perpendicular to the C_2 axis of the monomer. In contrast to the recent *ab initio* calculations by Bulski *et al.* and by Chalisinski *et al.*, the AW2 minimum is more nearly hydrogen bonded rather than antihydrogen bonded. On the AW2 surface, the minimum of 142.98 cm^{-1} occurs at ($R=3.636$ Å, $\theta=74.3°$, $\phi=0°$). Internal rotation of the water monomer is hindered by barriers to internal rotation in the plane at $\theta=0°$ and 180° and to out of plane rotation at $\theta=90°$, $\phi=90°$. Along the minimum energy pathway, barriers to in-plane rotation of 26.3 cm^{-1} ($R=3.702$ Å, $\theta=0°$, $\phi=0°$) and 17.2 cm^{-1} ($R=3.518$ Å, $\theta=180°$, $\phi=0°$) are present. The barrier to out-of-plane rotation is much larger, 54.2 cm^{-1} at ($R=3.671$ Å, $\theta=200.7°$, $\phi=90°$).

Both strong attractive and repulsive forces operating in the vicinity of the hydrogen atom are evident in the shape of the AW2 IPS. At intermolecular separations longer than 3.8 Å, the attractive forces dominate and the potential minimum occurs at the linear hydrogen bonded geometry with all four atoms coplanar. In the repulsive region of the surface ($R<3.5$ Å) the preferred orientations have the argon located in the monomer plane in the antihydrogen bonded configurations $\theta=125°$. At intermediate intermolecular separations, the competition between the attractive forces favoring hydrogen bonding and the repulsive wall of the hydrogen atom results in a transitional region. In $Ar-H_2O$ this transitional region occurs precisely in the region most extensively sampled by the bound states. Thus angular–radial coupling is an essential feature of the dynamics of this system. Since the strongest coupling of angular and radial degrees of freedom occurs in the region of the minimum on the AW2 IPS, this aspect of the potential is especially well determined.

The structure of the IPS for $Ar-H_2O$ can be understood by extension of the rationale for the structure in Rg–HX complexes presented by Hutson.[3] In each of the Rg–HX systems, the effect of the hydrogen atom is to reduce electron density, and consequently repulsion, at the linear orientation Rg–XH. As a result, the Rg–HX systems are characterized by a primary minimum favored by attractive forces, at the hydrogen bonded geometry Rg–HX and a secondary minimum favored by reduced repulsion in the antihydrogen bonded geometry, Rg–XH. The similarities to Rg–HX systems can be seen in Fig. 2, which shows the IPS perpendicular to the monomer plane. Ignoring structural details, this cut through the AW2 IPS can be considered a Rg–HO potential, analogous to the Rg–HX systems. In this figure, we see the now familiar double minimum structure of the Rg–HX potentials. However, the primary minimum is at the oxygen end—not at the hydrogen end. We speculate that this is due to the presence of *two* hydrogens. The electron withdrawing effect is increased by the presence of two hydrogens, further reducing the repulsive forces at the $Rg-OH_2$ configuration. This geometry becomes 9.1 cm^{-1} more stable than the $Ar-H_2O$ geometry, which is quite strongly favored by attractive forces. We can also take the structure of the molecule into account. If we compare energies along the OH bond vector instead of along the symmetry axis, the ordering of the favored orientations is reversed. Approach along the OH bond in the hydrogen bonded orientation Ar–HO is favored by 7.7 cm^{-1} over the antihydrogen bonded approach Ar–OH. However, the rationale for this result is unchanged from that given above, with the exception that the attractive forces favor approach along the hydrogen bond more strongly than between the two hydrogen atoms, and that the repulsive forces are even further weakened at the antihydrogen bonded geometry.

The strong protrusion of the hydrogen atom beyond the spherical repulsion surrounding the monomer in the $Ar-H_2O$ IPS is somewhat surprising. There is little evidence for structure due to the extension of the hydrogen atom beyond a spherical repulsion surrounding the fluorine atom in the Ar–HF ($v=1$) IPS derived by Nesbitt *et al.*[54] from a fit to an extensive set of VRT data. On this IPS, the argon to HF center of mass distance at the potential minimum is 3.40 Å at both the Ar–HF and the Ar–FH geometries. Along the OH bond vector, the AW2 IPS has a minimum at $R=3.71$ Å in the Ar–HO orientation and 3.46 Å in the Ar–OH orientation. In the plane of the monomer, the potential minimum occurs closest to the center of mass ($R_m=3.46$ Å) at $\theta=125°$ and it is farthest from the center of mass ($R_m=3.73$ Å) at $\theta=49°$. The reasons for this difference between $Ar-H_2O$ and Ar–HF arise from many competing effects. Fluorine has a smaller van der Waals radius than oxygen, which should make the protrusion of the hydrogen more pronounced in Ar–HF, the opposite of what is observed. The OH bond in water (0.9724 Å) is longer than the HF bond (0.9263 Å), contributing to the protrusion. The presence of two hydrogen atoms rather than one reduces the repulsion at the Ar–OH geometry, perhaps giving the appearance of an extended hydrogen atom. Finally, the electronegativity of fluorine is larger than that of oxygen, preventing as much electron withdrawal in HF as can occur in H_2O.

Although the AW2 IPS has been extracted exclusively from spectroscopic data, the final test of any model potential surface will be its ability to simultaneously reproduce a wide variety of experimental phenomena (e.g., pressure broadening cross sections, virial coefficients, differential scattering cross sections, solubilities, phase diagrams, $\cdots$) that depend on the intermolecular forces. Recent efforts by Green, and co-workers[55–57] to accurately compute pressure broadening cross sections on IPS which have been derived from VRT data provide one such test. For instance, comparison of measured pressure broadening cross-sections for HCl rotational lines, broadened by argon, with those computed on the H6(3) surface,[56] are generally in excellent agreement. Only the low temperature broadening of the $J=1\leftarrow 0$ line is computed to be outside the error bars of the experimental measurements. This line is computed to be 15% (more than five times the experimental error bars)

from the experimental values at low temperature. For Ar–H_2O, the pressure broadening cross sections computed[55] using the AW1 surface give both the correct magnitude and temperature dependence for all of the different rotational lines tested, but they are all uniformly about 15% higher (three times the experimental error bars) than the experimental values. Green has suggested that the disagreement could be the result of having too little anisotropy in the slope of the repulsive wall (β) of the IPS. These terms were constrained to be zero both in the AW1 and in the AW2 surface, since the spectroscopic data are insensitive to anisotropy in β smaller than 0.2 $Å^{-1}$ or so.

The AW2 IPS reproduces the qualitative picture of the anisotropic intermolecular forces presented by Chalisinski *et al.*[22] and Bulski *et al.*[23] However, there remain significant quantitive differences between the two *ab initio* calculations and the experimental IPS. While the AW2 surface has a minimum with a similar binding energy to that obtained *ab initio*, the position of the minimum and the shape of the potentials are not in agreement. The decrease in the overall anisotropic well depth on the AW2 surface from its value of $D_e=174$ cm^{-1} on the AW1 surface to 142.98 cm^{-1} is almost entirely due to the decrease in ϵ_{00}. This new well depth is still 10% deeper than the estimate of Chalisinski *et al.*[12] [$D_e=130$ cm^{-1}], who scaled their *ab initio* result of $D_e=108$ cm^{-1} by 25%, and 10% shallower than the 157 cm^{-1} binding energy computed by Bulski *et al.* Comparison to other aspects of these calculations requires care because of the differences in coordinate systems used. Bulski *et al.* use a coordinate system with the origin at the H_2O center of mass, but choose the positive z direction to point from the hydrogens toward the oxygen. As a result, our θ corresponds to 180°-θ in the coordinates of Bulski *et al.*, and odd spherical harmonic terms in the well depth expansion have opposite signs in their work and ours. The *ab initio* calculations of Chalisinski *et al.* were performed at fixed separation of the heavy atoms, with R defined as the Ar–oxygen distance, and with $\theta=0$ at the Ar–OH_2 configuration (our $\theta=180°$). The barriers along the minimum energy path are not even approximately accessed in these *ab initio* calculations, as they would be in calculations performed at a fixed distance from the center of mass. Transforming their results to our coordinate system, in-plane barriers for rotation of the water of 35 cm^{-1} at ($R=3.68$ Å, $\theta=0°$, $\phi=0°$) and 10 cm^{-1} at ($R=3.82$ Å, $\theta=180°$, $\phi=0°$) relative to the energy at ($R=3.78$ Å, $\theta=101°$, $\phi=0°$) are indicated by the *ab initio* calculation. The energy differences between the same points on the AW2 IPS are nearly zero. Both *ab initio* calculations appear to overestimate the ratio of the repulsive forces to the attractive forces near the hydrogen atom. As a result, they produce a global minimum of approximately the same energy and position as the short range minimum on the AW2 surface, but do not find the global minimum indicated by our fit to the experimental data.

The slight bump that occurs in the repulsive wall of the AW2 IPS at $\theta=125°$, $\phi=90°$ is quite interesting. Localized lone pairs would produce repulsive anisotropy in this region of the IPS. No evidence is found in the *ab initio* calculations of Chalisinski *et al.* for the effects of localized lone pairs in the intermolecular potential. However, because the contributions of R_m^{30} and R_m^{32} are poorly determined, and because the effects of truncating the expansion in R_m no doubt have the largest impact on these two terms, we cannot presently say with confidence that the AW2 surface does unambiguously evidence the influence of localized lone pairs. Nonetheless, there is some preliminary indication that the experimental data are sensitive to the shape of the potential in the lone pair region, and that effects of localized lone pairs might be reflected in the data. It will be interesting to see if determination of additional terms in this expansion reduces or enhances the structure in this region of the IPS, and if additional data can confirm or deny the influence of the lone pairs on the intermolecular interaction.

Additional spectroscopic measurements will provide a precise test of the accuracy of the AW2 IPS developed here, and will permit further details of the intermolecular forces in this system to be elucidated. In Table VIII we summarize predictions made for the strongest VRT bands which have not yet been observed and the values of VRT transitions which were not included in the AW2 fits either because their information content was largely redundant or because the additional computational expense did not appear to be justified. All of the observed transitions are in reasonable agreement with the values calculated on the AW2 surface, justifying the supposition that they do not contain significant new information. However, it should be noted that including this additional data might serve the purpose of reducing the uncertainty and the correlations in some of the parameters. New VRT bands will be far more valuable. Transitions to the $n=2$, $\Sigma(0_{00})$ and $n=2$, Σ, and $\Pi(1_{01})$ and the $\Delta(2_{12})$ the states of Ar–H_2O are all likely to be observable with current technology. Among the most important measurements will be those that constrain the dissociation energy. Some of these states are sufficiently close to dissociation that high J transitions may exhibit predissociation. Calculations of the lifetimes of these levels would be a valuable guide to experimentalists. Direct calculations on a model IPS have proven valuable in interpreting experimental data on predissociation in Ar–HCl.[8,46] If predissociation can be observed, it would provide an exact measure of the van der Waals bond energy. Even if all the transitions observed are bound, measurement of these transitions may provide a more precise lower limit to the binding energy than is currently available. There are also many strong Ar–D_2O transitions associated with $j=2$ internal rotor states and $n=1$ stretching levels. These states are strongly affected by angular –radial coupling and would serve as a stringent test of the accuracy of the AW2 IPS. These transitions might also provide more precise constraints on the T_{30} and T_{32} anisotropies, and perhaps other constants as well. Measurements of the quadrupole hyperfine structure, the dipole moment or transition moments would also provide valuable con-

TABLE VIII. Spectroscopic predictions on the AW2 surface. See Table VI for predictions of transition moments and quadrupole coupling constants.

		Experiment	Calculated	Residuals
Ar–H_2O				
$J=1\leftarrow0$				
$n=2,\Sigma(0_{00})$	$A_1\leftarrow A_2$		5 048.6	
$\Sigma(2_{12})$	$B_1\leftarrow B_2$		4 580.1	
$n=2,\Sigma(1_{01})$	$B_1\leftarrow B_2$		5 349.0	
$J=1\leftarrow1$				
$\Pi(1_{11})$	$A_1\leftarrow A_2$	2 51.2	248.3	2.9
$n=1,\Pi(1_{10})$	$B_2\leftarrow B_1$		123.1	
$n=2,\Pi(1_{01})$	$B_2\leftarrow B_1$		273.2	
$J=2\leftarrow1$				
$\Sigma(0_{00})$	$A_1\leftarrow A_2$	11 950.1	11 952.5	−2.4
$n=1,\Sigma(0_{00})$	$A_1\leftarrow A_2$	11 351.4	11 349.7	1.8
$\Pi(1_{11})$	$A_2\leftarrow A_1$	11 977.7	11 971.5	6.2
$\Sigma(1_{11})$	$A_1\leftarrow A_2$	11 945.3	11 948.5	−3.2
$n=2,\Sigma(0_{00})$	$A_1\leftarrow A_2$		10 094.9	
$\Sigma(1_{01})$	$B_2\leftarrow B_1$	11 647.0	11 654.3	−7.0
$\Pi(1_{01})$	$B_2\leftarrow B_1$	12 214.2	12 211.6	2.6
$\Pi(1_{10})$	$B_2\leftarrow B_1$	12 148.9	12 160.3	−11.4
$n=1,\Sigma(1_{01})$	$B_2\leftarrow B_1$	10 920.6	10 892.9	27.1
$\Sigma(1_{10})$	$B_1\leftarrow B_2$	12 103.0	12 088.7	14.3
$n=1,\Pi(1_{01})$	$B_2\leftarrow B_1$	11 132.5	11 142.31	−9.8
$n=1,\Pi(1_{10})$	$B_2\leftarrow B_1$		11 083.6	
$n=1,\Pi(1_{10})$	$B_1\leftarrow B_2$		10 837.5	
$\Sigma(2_{12})$	$B_2\leftarrow B_1$		9 206.2	
$\Pi(2_{12})$	$B_2\leftarrow B_1$	12 577.2	12 489.0	88.3
$n=2,\Sigma(1_{01})$	$B_2\leftarrow B_1$		10 710.0	
$n=2,\Pi(1_{01})$	$B_2\leftarrow B_1$		10 333.4	
$n=2,\Pi(1_{01})$	$B_1\leftarrow B_2$		9 784.0	
$J=2\leftarrow2$				
$\Pi(1_{11})$	$A_2\leftarrow A_1$	762.5	745.3	14.7
$\Pi(1_{01})$	$B_2\leftarrow B_1$	614.4	612.7	1.8
$\Pi(1_{10})$	$B_2\leftarrow B_1$	440.3	440.2	0.2
$n=1,\Pi(1_{01})$	$B_2\leftarrow B_1$	541.2	544.0	−4.0
$\Pi(2_{12})$	$B_2\leftarrow B_1$	1 939.7	1 866.8	72.9
$\Delta(2_{12})$	$B_2\leftarrow B_1$		2.62	
VRT bands (GHz)				
$n=2,\Sigma(0_{00})\leftarrow\Sigma(0_{00})$	$A_2\leftarrow A_1 J=1\leftarrow0$		1 776.13	
$\Sigma(2_{12})\leftarrow\Sigma(1_{01})$	$B_1\leftarrow B_2 J=1\leftarrow0$		1 700.67	
$n=2,\Sigma(1_{01})\leftarrow\Sigma(1_{01})$	$B_1\leftarrow B_2 J=1\leftarrow0$		1 972.03	
$n=2,\Pi(1_{01})\leftarrow\Sigma(1_{01})$	$B_1\leftarrow B_2 J=1\leftarrow0$		2 130.67	
$n=1,\Sigma(1_{10})\leftarrow\Pi(1_{01})$	$B_1\leftarrow B_2 J=2\leftarrow1$		1 715.73	
$\Delta(2_{12})\leftarrow\Pi(1_{01})$	$B_2\leftarrow B_1 J=2\leftarrow1$		1 756.83	
Ar–D_2O				
$J=1\leftarrow0$				
$n=1,\Sigma(0_{00})$	$A_1\leftarrow A_2$		3 972.0	
$\Sigma(2_{02})$	$A_1\leftarrow A_2$		6 589.3	
$\Sigma(2_{12})$	$B_1\leftarrow B_2$		4 934.9	
$n=1,\Sigma(1_{01})$	$B_1\leftarrow B_2$		5 713.8	
$J=1\leftarrow1$				
$\Pi(1_{11})$	$A_1\leftarrow A_2$	1 201.0[c]	1 155.2	45.8
$\Pi(2_{02})$	$A_1\leftarrow A_2$		168.6	
$\Pi(1_{01})$	$B_1\leftarrow B_2$	163.3[d]	162.3	1.0
$\Pi(1_{10})$	$B_1\leftarrow B_2$	133.9[d]	139.4	−5.5
$\Pi(2_{12})$	$B_1\leftarrow B_2$		−98.7	
$J=2\leftarrow1$				
$\Sigma(0_{00})$	$A_1\leftarrow A_2$	11 180.8[b]	11 178.2	2.6
$\Sigma(1_{11})$	$A_1\leftarrow A_2$	13 453.8[c]	13 372.5	81.3
$\Pi(1_{11})$	$A_1\leftarrow A_2$	8 949.3[c]	9 012.5	−63.2
$\Pi(1_{11})$	$A_2\leftarrow A_1$	11 171.8[c]	11 159.4	12.4
$n=1,\Sigma(0_{00})$	$A_1\leftarrow A_2$		13 159.9	
$\Sigma(2_{02})$	$A_1\leftarrow A_2$		8 071.9	

TABLE VIII. (*Continued.*)

		Experiment	Calculated	Residuals
$\Pi(2_{02})$	$A_1 \leftarrow A_2$		11 066.2	
$\Sigma(1_{01})$	$B_2 \leftarrow B_1$	10 914.8[b]	10 907.6	7.2
$\Pi(1_{01})$	$B_1 \leftarrow B_2$	10 931.5[d]	10 927.1	4.4
$\Pi(1_{10})$	$B_1 \leftarrow B_2$	11 196.5[d]	11 193.7	2.8
$\Sigma(2_{12})$	$B_2 \leftarrow B_1$		9 878.1	
$\Pi(2_{12})$	$B_1 \leftarrow B_2$		10 671.5	
$n=1,\Sigma(1_{01})$	$B_2 \leftarrow B_1$		11 432.8	
$J=2\leftarrow 2$				
$\Pi(1_{11})$	$A_2 \leftarrow A_1$	3 424.5[c]	3 302.2	122.3
$\Pi(2_{02})$	$A_2 \leftarrow A_1$		−389.7	
$\Pi(1_{01})$	$B_2 \leftarrow B_1$	489.1[d]	485.9	3.2
$\Pi(1_{10})$	$B_2 \leftarrow B_1$	401.8[d]	418.2	−16.4
$\Pi(2_{12})$	$B_2 \leftarrow B_1$		−317.2	
$\Delta(2_{12})$	$B_2 \leftarrow B_1$		3.2	
VRT bands (GHz)				
$\Sigma(2_{02})\leftarrow\Sigma(0_{00})$	$A_2\leftarrow A_1 J=1\leftarrow 0$		967.24	
$\Pi(2_{02})\leftarrow\Sigma(0_{00})$	$A_2\leftarrow A_1 J=1\leftarrow 0$		1 043.24	
$n=1,\Sigma(0_{00})\leftarrow\Sigma(0_{00})$	$A_2\leftarrow A_1 J=1\leftarrow 0$		1 092.79	
$\Sigma(1_{10})\leftarrow\Pi(1_{01})$	$B_1\leftarrow B_2 J=2\leftarrow 1$		528.59	
$\Sigma(2_{12})\leftarrow\Sigma(1_{01})$	$B_1\leftarrow B_2 J=1\leftarrow 0$		882.93	
$\Pi(2_{12})\leftarrow\Sigma(1_{01})$	$B_1\leftarrow B_2 J=1\leftarrow 0$		1 080.33	
$n=1,\Sigma(1_{01})\leftarrow\Sigma(1_{01})$	$B_1\leftarrow B_2 J=1\leftarrow 0$		1 092.79	
$\Delta(2_{12})\leftarrow\Pi(1_{01})$	$B_1\leftarrow B_2 J=2\leftarrow 1$		892.33	

[a]Experimental data from Refs. 13, 16, and 20 except where noted.
[b]Reference 25.
[c]Reference 26.
[d]Reference 27.

straints. Predictions for these expectation values are also given in Table VI.

SUMMARY

We have derived a detailed and precise IPS for the Ar–H_2O complex by a direct fit of a 12 parameter model to 37 VRT measurements. The measurements include the positions of 14 VRT bands, and 15 rotational term values for two isotopes, as well as the ground state dipole moment and the quadrupole hyperfine coupling constants in the ground and first excited states of Ar–H_2O. The AW2 IPS describes intermolecular forces which reflect the full topological complexity of the water molecule. Both the attractive and repulsive anisotropic forces are shown to be large and to exhibit a truly remarkable level of cancellation near the potential minimum. It is small variations in the extent of this cancellation which is responsible for the rapid variation of the optimum orientation with distance from the center of mass in the region of the potential minimum. Because of this substantial angular–radial coupling, approximate methods of studying the intermolecular dynamics that depends on separation of variables are grossly inadequate. We have employed the collocation method to rigorously solve for the eigenvalues and eigenvectors of the three-dimensional Hamiltonian describing the intermolecular dynamics of Ar–H_2O with a minimum of approximations—we assume a finite basis set is adequate, and that the intermolecular dynamics are separable from the intramolecular vibrational motion. Improvements to the rate of convergence and stability of this method have been described.

The insights derived from the work described herein can be applied to enhance our understanding of a wide array of phenomena which depend on intermolecular forces. Modeling the solvation of nonpolar species (such as a rare gas) in liquid H_2O continues to be of great interest. The AW2 IPS represents a very accurate model of the rare gas–H_2O interaction. This potential will also be useful in the modeling of energy transfer in collisions of Ar and H_2O, and in the study of predissociation of vibrationally excited Ar–H_2O complexes. Lascola and Nesbitt have studied vibrationally excited Ar–H_2O,[17] and Clary[58] has found a preliminary version of this IPS gives excellent agreement with predissociation rates measured by Nesbitt and co-workers. More generally, it will be possible to extract atom–atom repulsive (and possibly attractive) forces from the now accurately determined Ar–H_2,[3] Ar–HF,[7] Ar–HCl,[8] Ar–H_2O and and Ar–NH_3 (Ref. 9) IPS. A precise range for the repulsive forces surrounding the hydrogen atom could then be derived. These atom–atom forces could then be fruitfully employed in the many computer models which have van der Waals forces represented as a sum of atom-atom attractive and repulsive terms. It would also be interesting to try to remove the effects of the argon atom, and then to see if the repulsive force field surrounding the water monomer and the permanent moments of water can be used to build an accurate water dimer potential—one which is firmly constrained by experimental properties of H_2O embedded in a molecular complex.

The FORTRAN potential subroutine used to define the AW2 IPS is available from the authors upon request.

ACKNOWLEDGMENTS

The authors are grateful to C. A. Schmuttenmaer for numerous helpful discussions. This work was supported through the Experimental Physical Chemistry Program of the National Science Foundation (Grant No. CHE-9123335).

[1] R. C. Cohen and R. J. Saykally, J. Phys. Chem. **96**, 1024 (1992).
[2] R. C. Cohen and R. J. Saykally, Annu. Rev. Phys. Chem. **42**, 381 (1991).
[3] J. M. Hutson, Annu. Rev. Phys. Chem. **41**, 123 (1990).
[4] R. C. Cohen and R. J. Saykally, J. Phys. Chem. **94**, 7991 (1990).
[5] R. A. Aziz and H. H. Chen, J. Chem. Phys. **67**, 5719 (1977); R. A. Aziz, J. Presley, U. Buck, and J. Schleusener, *ibid.* **70**, 4737 (1979).
[6] A. R. W. Mckellar, J. Chem. Phys. **92**, 3261 (1990); S. Green, *ibid.* **92**, 4679 (1992), and references therein.
[7] J. M. Hutson, J. Phys. Chem. **96**, 4237 (1992).
[8] J. M. Hutson, J. Chem. Phys. **96**, 6752 (1992).
[9] C. A. Schmuttenmaer *et al.* (in preparation).
[10] M. J. Elrod, D. W. Steyert, and R. J. Saykally, J. Chem. Phys. **94**, 58 (1991); **95**, 3182 (1991).
[11] L. Dore, M. E. Elrod, R. C. Cohen, C. A. Schmuttenmaer, K. L. Busarow, and R. J. Saykally (in preparation).
[12] J. G. Loeser, C. A. Schmuttenmaer, R. C. Cohen, M. J. Elrod, R. J. Saykally, R. E. Bumgarner, and G. A. Blake, J. Chem. Phys. **97**, 4727 (1992).
[13] R. C. Cohen, K. L. Busarow, Y. T. Lee, and R. J. Saykally, J. Chem. Phys. **92**, 169 (1990).
[14] B. Guillot, Y. Guissani, and S. Bratos, J. Chem. Phys. **95**, 3643 (1991); H. Takanaka and K. Takanishi, *ibid.* **95**, 3719 (1991); T. Lazardis and M. E. Paulaitis, J. Phys. Chem. **96**, 3847 (1992).
[15] J. Ree and H. K. Shin, Chem. Phys. Lett. **193**, 215 (1992), and references therein.
[16] R. C. Cohen and R. J. Saykally, J. Chem. Phys. **95**, 7891 (1991).
[17] R. Lascola and D. J. Nesbitt, J. Chem. Phys. **95**, 7917 (1991).
[18] C. A. Schmuttenmaer, R. C. Cohen, J. G. Loeser, and R. J. Saykally, J. Chem. Phys. **95**, 9 (1991).
[19] A. L. Cooksy, S. Drucker, J. Faeder, C. A. Gottlieb, and W. Klemperer, J. Chem. Phys. **90**, 3017 (1991); K. R. Leopold, G. T. Fraser, F. J. Lin, D. D. Nelson, and W. Klemperer, *ibid.* **81**, 4922 (1984), and references therein.
[20] R. C. Cohen, K. L. Busarow, K. B. Laughlin, G. A. Blake, M. Havenith, Y. T. Lee, and R. J. Saykally, J. Chem. Phys. **89**, 4494 (1988).
[21] J. M. Hutson, J. Chem. Phys. **92**, 157 (1990).
[22] G. Chalisinski, M. M. Szczesniak, and S. Scheiner, J. Chem. Phys. **94**, 2807 (1991).
[23] M. Bulski, P. E. S. Wormer, and A. Van der Avoird, J. Chem. Phys. **94**, 8097 (1991).
[24] M. Bulski, P. E. S. Wormer, and A. Van der Avoird, J. Chem. Phys. **94**, 491 (1991).
[25] G. T. Fraser, F. J. Lovas, R. D. Suenram, and K. T. Matsumura, J. Mol. Spectrosc. **144**, 97 (1990).
[26] S. Suzuki, R. E. Bumgarner, P. A. Stockman, P. G. Green, and G. A. Blake, J. Chem. Phys. **94**, 824 (1991).
[27] E. Zwart and W. L. Meerts, Chem. Phys. **151**, 407 (1991).
[28] K. T. Tang and J. P. Toennies, J. Chem. Phys. **80**, 3726 (1984).
[29] J. M. Hutson, J. Chem. Phys. **89**, 4550 (1988).
[30] C. G. Gray and K. E. Gubbins, *Theory of Molecular Fluids: Vol. 1* (Clarendon, Oxford, 1984).
[31] A. Van der Avoird, P. E. S. Wormer, F. Muldur, and R. M. Berns, Top. Curr. Chem. **93**, 1 (1980).
[32] T. R. Dyke and J. S. Muenter, J. Chem. Phys. **59**, 3125 (1976).
[33] J. Verhoeven and A. Dymanus, J. Chem. Phys. **52**, 3222 (1970).
[34] W. F. Murphy, J. Chem. Phys. **67**, 5877 (1977).
[35] K. T. Tang, J. M. Norbeck, and P. R. Certain, J. Chem. Phys. **64**, 3063 (1976); E. A. Reinsch and W. Meyer, Phys. Rev. A **14**, 915 (1976).
[36] A. D. Buckingham, P. W. Fowler, and J. M. Hutson, Chem. Rev. **88**, 963 (1988).
[37] *CRC Handbook of Chemistry and Physics*, 73rd ed. (CRC Press, Boca Raton, FL, 1992).
[38] J. W. Johns, J. Opt. Soc. Am. B **2**, 1340 (1985).
[39] F. C. De Lucia and P. Helminger, J. Mol. Spectrosc. **70**, 263 (1978).
[40] R. Bhattacharjee, J. S. Muenter, and M. D. Marshall, J. Mol. Spectrosc. **145**, 302 (1991).
[41] W. Rijks and P. E. S. Wormer, J. Chem. Phys. **90**, 6507 (1989); **92**, 5754 (1990).
[42] R. J. Leroy and J. M. Hutson, J. Chem. Phys. **86**, 837 (1987).
[43] J. M. Hutson, Adv. Mol. Vib. Collision Dyn. **1**, 1 (1991).
[44] S. E. Choi and J. C. Light, J. Chem. Phys. **92**, 2129 (1990); M. Mladenovic and Z. Bacic, *ibid.* **94**, 4988 (1991).
[45] J. C. Light, R. M. Whitnell, T. J. Park, and S. E. Choi, *Supercomputer Algorithms for Reactivity, Dynamics and Kinetics of Small Molecules*, NATO ASI Series C, Vol. 277, edited by A. Lagana (Kluwer, Dortdrecht, 1989), p. 187.
[46] D. C. Clary and P. J. Knowles, J. Chem. Phys. **93**, 6334 (1990); D. C. Clary and D. J. Nesbitt, *ibid.* **90**, 7000 (1989).
[47] A. C. Peet and W. Yang, J. Chem. Phys. **91**, 6598 (1989).
[48] W. Yang and A. C. Peet, Chem. Phys. Lett. **153**, 98 (1988).
[49] A. C. Peet and W. Yang, J. Chem. Phys. **90**, 1746 (1989).
[50] W. Yang and A. C. Peet, J. Chem. Phys. **92**, 522 (1990).
[51] R. J. LeRoy, J. S. Carley, and J. E. Grabenstetter, Faraday Discuss. Chem. Soc. **62**, 169 (1977).
[52] R. A. Friesner, J. Phys. Chem. **92**, 3091 (1988).
[53] W. Gordy and R. L. Cook, *Microwave Molecular Spectra* (Interscience, New York, 1975).
[54] D. J. Nesbitt, M. S. Child, and D. C. Clary, J. Chem. Phys. **90**, 4855 (1989).
[55] S. Green, J. Chem. Phys. **95**, 3888 (1991).
[56] S. Green, J. Chem. Phys. **92**, 4679 (1990).
[57] S. Green, D. J. DeFrees, and A. D. McLean, J. Chem. Phys. **94**, 1346 (1991).
[58] C. Bissonnette and D. C. Clary, J. Chem. Phys. **97**, 8111 (1992).